POLITECNICO DI TORINO

Master's Degree in Energy and Nuclear Engineering

Unified Momentum Model-based macrodynamic rotor modeling for floating offshore wind turbines in the Mediterranean Sea

Supervisor

Dr. Bruno Paduano

Candidate

Ardemia Acampora

Co-supervisors

Dr. Xiaoli Jiang
Ing. Davide Issoglio
Prof. Giovanni Bracco

March 2025

Abstract

Substantial growth in wind energy capacity is essential to meeting global mid-century net-zero carbon emissions targets. As wind turbines scale up and expand into offshore environments, they encounter operating conditions where traditional aerodynamic models often fail: high-thrust regions and yaw-misaligned winds. By leveraging a first-principles approach, the recently developed Unified Momentum Model (UMM) circumvents the limitations associated with the empirical corrections applied to the classical momentum theory-based models to predict rotor dynamics under these operating conditions. Replacing classical momentum theory, the UMM can be coupled with a traditional blade element model to obtain a Blade Element Momentum (BEM) that works across all operating regimes without empirical corrections. With the primary aim of verifying the UMM for the analysis of Floating Offshore Wind Turbines (FOWTs), this thesis develops a comparative analysis for a numerical case study based on the floating NREL 5-MW reference wind turbine in the spar configuration. For a preliminary analysis, the bottom fixed case is first considered. The power coefficient versus Tip Speed Ratio (TSR) curve is evaluated for different blade pitch angles in both fully aligned and yaw misaligned wind conditions leveraging three different thrust-induction momentum closures (classical momentum, classical momentum with high-thrust correction, and UMM) to the BEM. Findings indicate that traditional one-dimensional momentum theory without high-thrust modifications fails to converge when thrust coefficients exceed unity, limiting the determination of optimal control settings. In contrast, the other two momentum closures achieve convergence across all operating scenarios. However, only the UMM-based model yields an optimal control strategy predicting an increase in thrust levels under yaw misalignment in agreement with recent literature. With the aim to further verify the UMM for estimating the productivity of FOWTs, the analysis was extended to the floating case, considering metocean conditions related to the Pantelleria installation site in Italy, integrating the UMM within the Matlab for Offshore floating wind turbines Simulation Tool (MOST) framework. Results show that across all wind directions and for both BEM models, fixed configurations generally outperform floating ones in terms of productivity due to the dynamic response of floating platforms to ocean currents and waves.

While the UMM-integrated version of MOST generally shows improved productivity compared to the traditional BEM implementation, the trend is reversed for yaw angles exceeding 40°, suggesting the need for further analysis under varying yaw conditions. The higher computational cost of the UMM-integrated version of MOST is justified by its increased fidelity and ability to model wakes.

Acknowledgements

I would like to express my sincere gratitude to Dr. Xiaoli Jiang for welcoming me to TU Delft and for giving me the opportunity to spend some time abroad during my Master's program. Your precision and valuable feedback have been essential for this work.

I am also deeply thankful to Prof. Giovanni Bracco for teaching me the basics of wind turbines and for introducing me to the wonderful research group at MOREnergy Lab.

Speaking of MORE, my thanks extend to Ing. Davide Issoglio and Dr. Bruno Paduano, without whose support this work would not have been possible. Davide, I am grateful for your readiness to help me out during challenging times and for your insightful technical advice. Bruno, my deepest gratitude goes to you for your constant support, both technical and personal, and for your endless patience in teaching me even the simplest concepts.

Vorrei esprimere la mia sincera gratitudine alla Dott.ssa Xiaoli Jiang per avermi accolta alla TU Delft e per avermi dato l'opportunità di trascorrere del tempo all'estero durante il mio corso di Laurea magistrale. La sua precisione e i suoi preziosi consigli sono stati essenziali per questo lavoro.

Sono anche profondamente riconoscente al Prof. Giovanni Bracco per avermi insegnato le basi sulle turbine eoliche e per avermi introdotta nello splendido gruppo di ricerca al MOREnergy Lab.

Parlando del MORE, i miei ringraziamenti si estendono all'Ing. Davide Issoglio e al Dott. Bruno Paduano, senza il cui supporto questa tesi non sarebbe stata possible. Davide, ti sono grata per la tua disponibilità ad aiutarmi nei momenti più difficili e per i tuoi consigli tecnici. Bruno, la mia gratituidine più profonda va a te, per il tuo supporto costante, sia tecnico sia personale, e per la tua infinita pazienza nell'insegnarmi anche i concetti più semplici.

Table of Contents

List of Tables

List of Figures

Acronyms

ABL Atmospheric Boundary Layer

AEP Annual Energy Production

BEM Blade Element Momentum

CF Capacity Factor

CFD Computational Fluid Dynamics

ECMWF European Center for Medium-Range Weather Forecasts

FOWT Floating Offshore Wind Turbine

LCOE Levelized Cost Of Energy

MIT Massachusetts Institute of Technology

MORE Marine Offshore Renewable Energy

MOST Matlab for OFWT Simulation Tools

NREL National Renewable Energy Laboratory

OFWT Offshore Floating Wind Turbine

OPEX OPerational EXpenditure

RES Renewable Energy Sources

RMSE Root Mean Square Error

TLP Tension Leg Platform

TSR Tip Speed Ratio

UMM Unified Momentum Model

WIMBY Wind In My Backyard

List of symbols

a Axial induction factor

a' Angular induction factor

a_n Rotor-normal induction factor

a_{skew} Skewed wake induction factor

$\bar{a}$ Wave amplitude

A Surface

α Angle of attack

B Number of blades

β Wake (jet) spread rate

c Chord

C_d Airfoil drag coefficient

C_l Airfoil lift coefficient

C_n Normal force coefficient

C_P Power coefficient

C_T Thrust coefficient

C'_T Modified thrust coefficient

C_t Tangential force coefficient

χ Wake skew angle

D Actuator disk diameter

dir_m Mean wave direction

dr Stream tube thickness

E Wave energy density

ϵ Tolerance

η Wave elevation

F Tip loss correction factor

f_i Actuator disk body forcing in the i^{th} direction

F_D Drag force

F_L Lift force

F_N Force normal to the plane of rotation

F_T Force tangential to the circle

g Gravitational acceleration

g_x Nonlinear force field in the x direction

g_y Nonlinear force field in the y direction

Γ_0 Circulation at disk hub height

γ Yaw angle

$\bar{\gamma}$ Peak enhancement factor

H Wave height

$H_{1/3}$ Significant wave height

h Water depth

H_s Significant height of combined wind and swell

J Wave power density

K Skewed wake correction factor

k Wave number

λ Tip speed ratio

λ_r Local tip speed ratio

$\bar{\lambda}$ Wavelength

$\dot{m}$ Air mass flow rate

m Spectral moment

μ Radial position normalized by rotor radius

μ_{BEM} Standard deviation obtained with the traditional version of MOST

μ_{UMM} Standard deviation obtained with the UMM-integrated version of MOST

$\dot{m}_{side}$ Mass flow across the control volume

O_{en} Energy scatter

O_w Occurrence scatter

occ Occurrence

Ω Angular velocity of the wind turbine rotor

ω Angular velocity imparted to the flow stream

$\bar{\omega}$ Wave frequency

P Power extracted from the wind

p Pressure

φ Angle of relative wind

$\bar{\varphi}$ Wave phase

ψ Blade azimuth angle

Q Torque

r Radius of the annular volume

R Rotor radius

ρ Air density

$S(\bar{\omega})$ Wave energy spectrum

s Shear layer width

$\bar{s}$ Wave steepness

σ Blade solidity

σ_{BEM} Average value obtained with the traditional version of MOST

σ_{UMM} Average value obtained with the UMM-integrated version of MOST

T Thrust force

$\bar{T}$ Wave period

$T_{1/3}$ Significant wave period

T_p Peak wave period

θ_p Section pitch angle

$\theta_{p,0}$ Blade pitch angle at the tip

θ_t Blade twist angle

U Undisturbed wind speed

u Reduced velocity in the rotor plane

U_{rel} Relative wind velocity

u_{100} 100 m u-component of wind

u_e Characteristic relative velocity

u_s Characteristic shear layer velocity

u_4 Streamwise wake velocity

v_4 Lateral wake velocity

v_{100} 100 m v-component of wind

v_t Tangential velocity

v_x Axial velocity

w Inflow velocity

w_x Streamwise velocity deviation from the mean

w_y Lateral velocity deviation from the mean

x_0 Near-wake length

Chapter 1

Introduction

To meet the 1.5°C global warming threshold by 2030 and reach global net-zero carbon emissions by mid-century, the world will need at least 380 GW of offshore wind capacity by 2030 and 2,000 GW by 2050. This represents a five-fold increase and a 27-fold increase from the current capacity of 75.2 GW, respectively [1]. In 2023, Europe ranked second after China in new offshore wind installations, with 3.8 GW of new capacity [1]. However, the Mediterranean region contributed only a small fraction of this growth, despite its high potential for offshore wind generation (estimated at 3,261 TWh/year according to Faraggiana et al. [2]). 99% of European offshore wind capacity is currently represented by fixed-bottom offshore technology [3]. The adoption of floating wind turbines, which is critical for the Mediterranean's deep waters, could contribute significantly to closing the gap between potential and installed capacity. To harness this potential, a coordinated effort in research, development, and supportive legislation [1] is essential to enable the deployment of wind turbines designed specifically for the Mediterranean's unique conditions, including deeper waters and moderate wind speeds.

In tandem with the growth in offshore wind projects, recent trends in wind turbine design have pushed the limits of current modeling techniques. With increasing rotor diameters, taller hub heights, and more complex design and control strategies, the limitations of classical aerodynamic models have become evident [4, 5]. These models, derived from classical momentum theories of the late 19th and early 20th centuries, struggle under high-thrust or yaw-misaligned conditions, which are common in modern offshore turbines [6]. Therefore, improving aerodynamic models has become a priority for the scientific community to support the design and operational optimization of next-generation wind turbines.

[1] Please note that a standardized regulatory framework for offshore wind in the Mediterranean is not yet established [2]

Addressing these limitations, the Unified Momentum Model (UMM) offers a significant advancement in rotor modeling. The UMM is a first-principles-based approach that addresses the inherent weaknesses of classical models, offering a unified framework to link rotor thrust, yaw, and induction effects with outlet velocity and pressure. This model accurately predicts rotor performance without relying on empirical corrections, making it a robust foundation for wind turbine design and performance analysis [6]. When combined with Blade Element Momentum (BEM) theory, the UMM represents a new, improved basis that allows for a more accurate initial design phase. This simple aerodynamic model can be combined with an optimization algorithm, aiming to minimize the Levelized Cost Of Energy (LCOE), before proceeding to more advanced structural models, such as Finite Element Method (FEM) and Computational Fluid Dynamics (CFD) simulations, that are computationally more intensive [7].

The primary objective of this thesis is to verify the macrodynamic rotor model based on the UMM and to integrate it into a MATLAB-based open-access tool that supports future design applications. Although this model can be applied across various geographical contexts, it holds particular potential for optimizing blade design in the Mediterranean region. The goal is to establish a flexible numerical framework that enables parametric analysis, providing a foundation for future design optimization strategies. However, optimization itself lies outside the scope of this study.

The following chapters of this thesis are organized as follows:

- Chapter 2 presents a short overview of different FOWT platforms, employing a simple pros and cons approach;
- Chapter 3 provides a review of classical aerodynamic models, discussing their limitations and empirical corrections;
- Chapter 4 presents the UMM, detailing its derivation, core principles, and performance;
- Chapter 5 explains the adaptation of the macrodynamic rotor model, based on the UMM, into a MATLAB-based open-access tool and outlines the methodology for comparative analysis applied in this study;
- Chapter 6 presents the results of a case study scenario, divided into static analysis, comparative analysis to assess productivity, and time domain analysis, accompanied by a critical analysis of the findings;
- Chapter 7 concludes the research, summarizing key insights and discussing potential future developments.

Chapter 2

FOWT platforms

Before delving into the aerodynamic models' review, this chapter provides an overview of state-of-the-art floating structures for offshore wind systems, setting the stage for the design choices discussed in the case study in Chapter 5. Given the deep waters of the Mediterranean, where this thesis is geographically situated, only floating platforms are considered. This analysis is deemed appropriate since the choice of the substructure impacts the system dynamics. The content of this chapter is mostly based on [8] and [9].

Floating platforms are typically classified according to their method of achieving static stability into:

- Spar, which are ballast stabilised;
- Semi-submersible and Barge, both buoyancy stabilised;
- Tension Leg Platform (TLP), that are mooring stabilised.

These substructures provide the necessary restoring moments to counteract the aerodynamic forces induced by wind, that tend to tilt the whole platform. Hence, the design of these platforms focuses on maximizing hydrostatic stiffness to minimize roll and pitch motions.

The main design characteristics and operating principles of these floating platforms are:

- **Spar**: they consist of a heavy cylindrical structure made of steel or concrete. They utilise water or solid materials for ballasting to maintain stability by keeping the center of gravity under the center of buoyancy. Thanks to the large draft, spar platforms are stable. Their design is simple so they can be fabricated in series, and moorings consist of catenary. However, they are required to be assembled offshore, resulting in costly operations that require

expensive heavy-lift vessels, and their structure requires large quantities of steel and concrete.

- **Semi-submersible**: they feature three to five cylindrical columns connected by slender pontoons. Stability is achieved by maximizing the waterplane area to enhance buoyancy. Stability in roll and pitch increases with the distance between the columns. Semi-submersible platforms can be assembled onshore and only require conventional tugs for transport and assembly purposes. As for the Spar configuration, they also are coupled with catenary moorings. The main drawbacks of this substructure are the high structural mass and the complex fabrication, which results in an expensive design.

- **Barge**: they leverage their extensive waterplane area for stabilisation. For this reason, their diameter is much larger than their height. They are easy to install and cheap but strongly suffer wave impact.

- **TLP**: they are characterized by vertical moorings and a central column linked to tensioned mooring lines. Legs are usually cables. When inclined, the higher tension in the windward leg creates a restoring moment, that provides stability [10]. The structure is designed with excess buoyancy to pre-tension the mooring system. TLPs are cheap to manufacture but since they are not self-stable, they require additional support, making them difficult to install and raising overall costs above those of the other two platforms. Furthermore, they require specific seabed conditions for mooring installation.

2.1 Comparison and design choice

The main advantages and disadvantages of FOWT platforms are summarized in Table 2.1, providing a clear comparison of their suitability for various operational conditions. Figure 2.1, instead, shows a graphical representation of the substructures.

The choice of platform type depends on specific site conditions, water depth, available infrastructure, and met-ocean conditions. Semi-submersible substructures are suitable for shallower waters, especially when port facilities can support assembly and load-out, and are advantageous in challenging met-ocean conditions due to their higher tolerance to wave heights during installation. Spar-buoy platforms are ideal for very deep waters exceeding 100 meters and require protected areas for assembly and erection, offering good stability but limited application in shallower waters. TLPs are best used in intermediate water depths of 70-200 meters and require suitable port infrastructure for assembly and load-out, with favorable met-ocean conditions during installation due to the need for a larger weather window.

Table 2.1: Advantages and disadvantages of FOWT substructures. Adapted from [9].

Platform type	Advantages	Disadvantages
Spar	Easy to manufacture Small heave motions	Hard to tow out Offshore installation Heavy and large structure Large pitch and roll Large seabed footprint Small deck Very deep water needed
Semi-sub	Easy to tow out Easy to install Large deck Onshore installation possible	Difficult to manufacture Large seabed footprint Large heave motions
Barge	Easy to tow out Easy to install Large deck Onshore installation possible	Large seabed footprint Large heave motions
TLP	Small heave, roll and pitch motions Small seabed footprint Light and small structure	Not self-stable Dedicated installation vessel Expensive mooring system

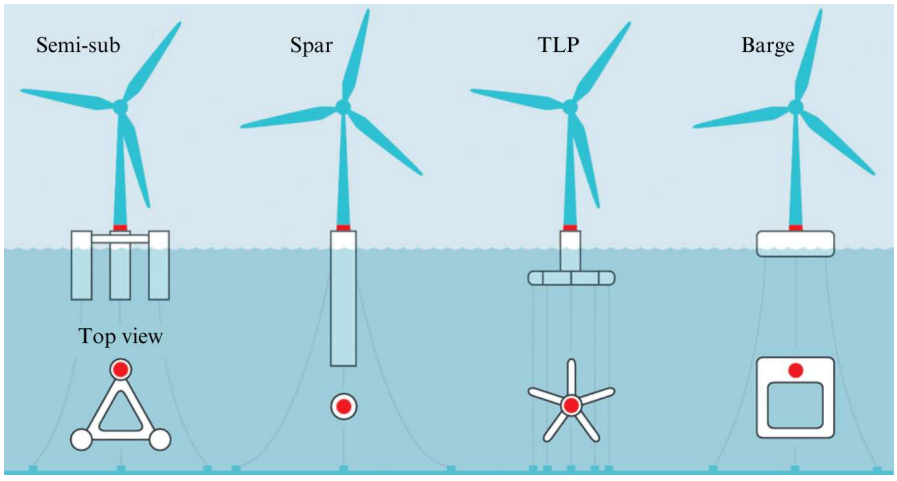

Figure 2.1: FOWT platforms. Adapted from [11].

Currently, there is not a single winning concept among the different FOWT substructures, and probably even in the future there will be a range of leading devices

suitable for different site conditions, and influenced by supply chain capabilities and local infrastructure [12]. Nevertheless, the Spar platform is the most cost-effective option for deep sea ($> 150\ m$) among the four major platform types [2]. It is also the only one recommended for water depths beyond $400\ m$ [12], making it particularly suitable for applications in the Mediterranean Sea, known for its steep bathymetric profile, where water depths can easily reach or even exceed this threshold. Moreover, Faraggiana et al. [2] specifically identify Spar platforms as the optimal choice for Italian maritime conditions, where the simulations site for this thesis will be selected. Given these considerations, it is claimed interesting to choose this type of platform configuration for the wind turbine that will be analysed in the case study detailed in Chapter 5.

Chapter 3

Background

The aerodynamic modeling of wind turbine rotors has historically depended on theories established in the late 19th and early 20th centuries. This chapter traces the evolution of these classical one-dimensional models, from 1D momentum equations to BEM formulation, examining their limitations and the empirical corrections that followed, ultimately arriving at the recent development of a unified model. This UMM, which is valid across all operating conditions of modern wind turbines, represents the central topic underpinning this thesis.

3.1 1D momentum equations

The 1D momentum theory, also known as the Rankine-Froude theory [13, 14, 15], was originally developed in the late 19th century for marine propulsion, but it is also applicable to wind turbine rotors, propellers, helicopters, and drones. This theory is at the core of a simple idealized wind turbine rotor model, generally attributed to Betz (1926) [16]. According to Rankine and Froude, the rotor is represented as a permeable disc that creates a discontinuity of pressure in the stream tube of air flowing through it. There is a uniformly distributed normal load across the rotor plane, resulting in a constant velocity profile in the wake. The integral of this load, representing the force of the wind on the rotor, is the total thrust force, T, as illustrated in figure 3.1. This theory is based on several simplifying hypotheses :

1. A control volume, whose boundaries are the surface of the stream tube and the 2 cross sections of the stream tube
2. the only flow is across the ends of the stream tube
3. the turbine is represented by a uniform actuator disc which creates a discontinuity of pressure in the stream tube of air flowing through it

4. an infinite number of blades constituting a disc
5. uniform thrust over the disc or rotor
6. the static pressure far upstream and downstream the rotor is equal to the undisturbed ambient static pressure
7. a non-rotating wake, therefore the fluid is laminar
8. constant air density

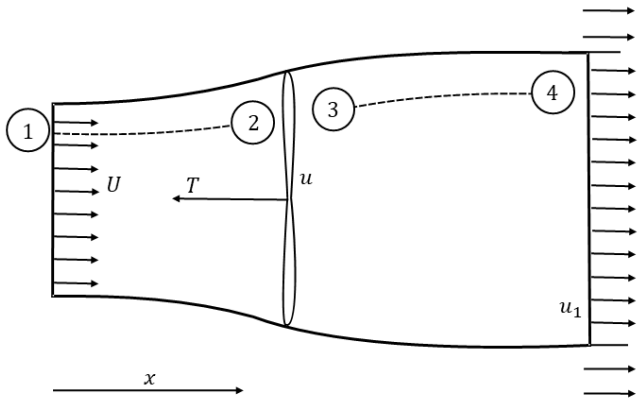

Figure 3.1: Representation of the rotor as a permeable disc.

The only flow affected by the thrust force is the one confined by the streamlines touching the rotor tip, while the free wind speed upstream is gradually reduced to a lower value in the wake. The induced velocities caused by the rotor's thrust are linked to the upstream and downstream velocities through the conservation of mass and momentum in one dimension perpendicular to the disk. According to Figure 3.1, the velocity due to the thrust force decreases with the downstream distance, and given that the mass flow is the same at any downstream plane, the streamlines have to expand. The undisturbed wind speed is U, the reduced velocity in the rotor plane is u and the velocity in the wake is u_1. The velocity in the rotor plane may also be written as:

$$u = (1 - a)U, \tag{3.1}$$

stating that velocity in the rotor plane is slowed down by a factor aU with respect to the undisturbed wind speed velocity, where a is the axial induction factor. This

factor expresses the difference between the undisturbed wind speed and the speed on the rotor, normalized by U. Its value can range between 0 and 0.5 (the latter is excluded), with higher values indicating a greater reduction of wind velocity behind the rotor. For hypotheses 2 and 6, the conservation of energy assuming no loss for the control volume confined by these is easily determined as:

$$P = \frac{1}{2}\dot{m}(U^2 - u_1^2) = \frac{1}{2}\rho u A(U^2 - u_1^2), \tag{3.2}$$

where $\dot{m}$ is the air mass flow rate, ρ is the air density, A the rotor area, and P is the power extracted from the wind. Applying Bernoulli between sections 1 to 2 and 3 to 4 of Figure 3.1 it is obtained:

$$p_0 + \frac{1}{2}\rho U^2 = p^+ + \frac{1}{2}\rho u^2, \tag{3.3}$$

$$p^- + \frac{1}{2}\rho u^2 = p_0 + \frac{1}{2}\rho u_1^2, \tag{3.4}$$

where p_0 is the ambient pressure, p^+ the pressure just upstream the rotor and p^- the pressure just behind the rotor. Combining the equations the pressure drop Δp over the rotor disc is obtained:

$$\Delta p = p^+ - p^- = \frac{1}{2}\rho(U^2 - u_1^2) = \frac{1}{2}\rho(U + u_1)(U - u_1). \tag{3.5}$$

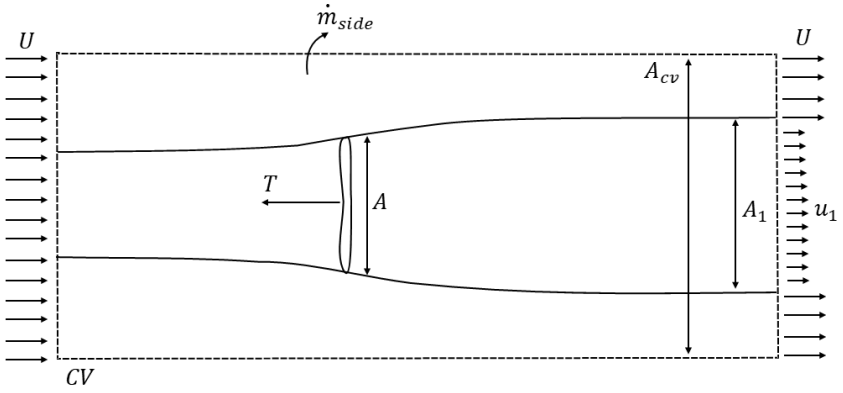

Figure 3.2: Cylindrical control volume enclosing the flow through an ideal wind turbine rotor.

Considering a cylindrical control volume (of surface A_{cv}) enclosing the flow through the rotor, as in Figure 3.2, the relationship between the flow and thrust force can be evaluated. The lateral boundary of this control volume is horizontal,

therefore the pressure around the control volume can only contribute to an axial force at the inlet and outlet planes, where the pressure is assumed to be equal to the ambient one. Consequently, the net pressure force is zero and the only remaining force in the flow direction is the unknown thrust force T. The lateral boundaries are no longer streamlines so there is a mass flow $\dot{m}_{side}$ crossing them, which is carrying axial momentum [7]. The conservation of axial momentum thus becomes:

$$-T = \rho A_1 U_1^2 + \rho(A_{cv} - A_1)U^2 + \dot{m}_{side}U - \rho A_{cv}U^2, \tag{3.6}$$

that combined with the mass conservation equation gives

$$\dot{m}_{side} = \rho A_{cv}U - \rho A_1 u_1 - \rho(A_{cv} - A - 1)U = \rho A_1(U - u_1), \tag{3.7}$$

thus resulting in

$$T = \rho A u(U - u_1). \tag{3.8}$$

Since the thrust can be expressed as the pressure drop over the rotor disc times the area, combining equations 3.5 and 3.8, the velocity in the rotor plane results in:

$$u = \frac{1}{2}(U + u_1). \tag{3.9}$$

The velocity in the wake is obtained by combining this expression with the rotor plane velocity definition expressed in Equation 3.1:

$$u_1 = (1 - 2a)U. \tag{3.10}$$

Finally, substituting this last expression in Equation 3.2, power can be expressed as:

$$P = 2\rho a(1 - a)^2 U^3 A, \tag{3.11}$$

and its coefficient as:

$$C_P = \frac{P}{\frac{1}{2}\rho U^3 A}. \tag{3.12}$$

Assuming one-dimensional flow and no losses the ideal power coefficient is obtained by substituting Equation 3.11 in Equation 3.12:

$$C_P = 4a(1 - a)^2. \tag{3.13}$$

The thrust coefficient is defined as:

$$C_T = \frac{T}{\frac{1}{2}\rho U^2 A}, \tag{3.14}$$

while its expression for an ideal rotor results from the combined use of the axial induction factor definition, Equation 3.8 and 3.9:

$$C_T = 4a(1 - a). \tag{3.15}$$

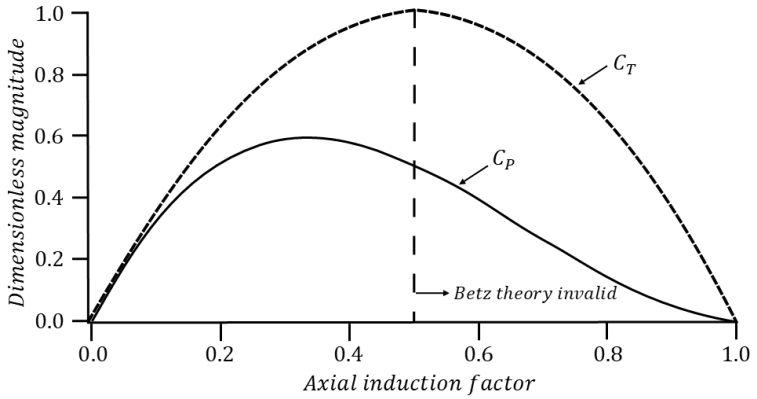

Figure 3.3: Power coefficient and thrust coefficient trends.

As illustrated in Figure 3.3, the maximum value of Equation 3.13 is $C_P = 16/27 \approx 0.59$ and occurs for $a = 1/3$. This point on the curve is known as the Betz limit: the maximum theoretically possible rotor power coefficient. In real cases, the maximum achievable power coefficient is lower due to:

- wake rotation behind the rotor;
- finite number of blades and associated tip losses;
- non-zero aerodynamic drag

The value of the thrust coefficient corresponding to the Betz limit is $C_T = 8/9 \approx 0.89$. The theory breaks down for axial induction factor values greater than $a = 0.5$ because of flow instability, backflow, and turbulence, which violate the initial assumptions 3.1. Instead, the theory can be applied to real rotors for values up to 10% higher than the optimal value of $a = 1/3$ [6]. For higher axial induction factors, empirical corrections are required, which will be discussed in Section 3.4.

3.2 Blade Element Momentum (BEM)

BEM theory, or strip theory, is one of the oldest and most common methods for calculating induced velocities on wind turbine blades. It relates the blade shape to the rotor's ability to extract power from the wind [16]. This theory, generally attributed to Betz and Glauert, originates from two different theories: blade element theory and a generalization of momentum theory that considers wake rotation.

3.2.1 Momentum theory

In the previous analysis of Section 3.1, it was assumed that no rotation was imparted to the flow. In reality, the rotation of a wind turbine rotor imparts an opposite rotation to the flow as a reaction to the torque that the flow exerts on the rotor. This wake rotation is shown in Figure 3.4. The generation of rotational kinetic

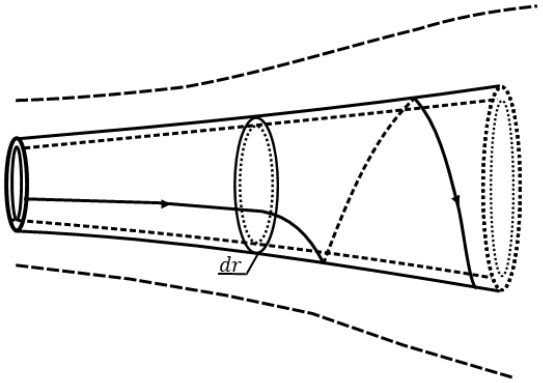

Figure 3.4: Stream tube of flow behind rotating wind turbine rotor.

energy in the wake results in less energy extraction by the rotor than would be expected without wake rotation. The extra kinetic energy in the wake will be higher if the generated torque is higher. Consequently, slow-running wind turbines experience more wake rotation losses than high-speed machines [16]. In this analysis, the control volume is an annular volume of radius r and thickness dr, as shown in Figure 3.5, resulting in a cross-sectional area equal to $2\pi r dr$. Pressure, wake rotation, and induction factors are all assumed to be functions of radius. Hypothesis

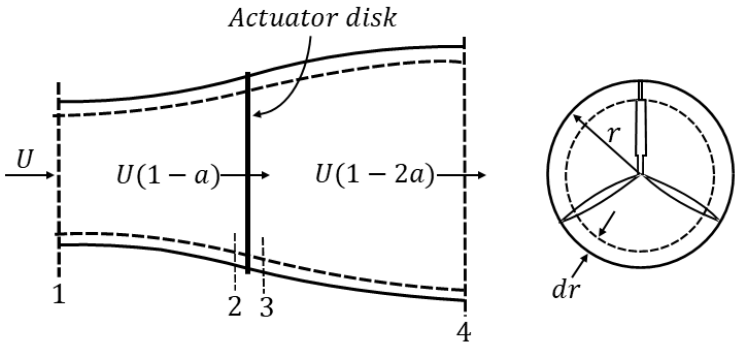

Figure 3.5: A stream tube of thickness dr intersecting the radial position r on the rotor plane.

6 of Section 3.1 is still valid if it is assumed that the angular velocity imparted to the flow stream ω is small compared to the angular velocity Ω of the wind turbine rotor. Applying the energy equation and considering that the angular velocity of the air relative to the blade increases from Ω to $\Omega + \omega$ while the axial component of velocity stays constant, an expression for the pressure difference across the blades is derived [1]:

$$p_2 - p_3 = \rho\left(\Omega + \frac{1}{2}\omega\right)\omega r^2. \tag{3.16}$$

An angular induction factor a' is defined as:

$$a' = \frac{\omega}{2\Omega}. \tag{3.17}$$

Considering that, by including wake rotation, the induced velocity at the rotor consists of both the axial component Ua and of a component in the rotor plane $r\Omega a'$, the expression for the thrust becomes:

$$dT = 4a'(1 + a')\frac{1}{2}\rho\Omega^2 r^2 2\pi r dr. \tag{3.18}$$

Given that the thrust on an annular cross-section can also be determined, by applying the linear momentum conservation equation, as a function of the axial induction factor a:

$$dT = 4a(1 - a)\frac{1}{2}\rho U^2 2\pi r dr, \tag{3.19}$$

the two expressions for thrust can be equated resulting in:

$$\frac{a(1 - a)}{a'(1 + a')} = \frac{\Omega^2 r^2}{U^2} = \lambda_r^2, \tag{3.20}$$

where λ_r is the local tip speed ratio. The tip speed ratio λ (or TSR) is defined as the ratio of the blade tip speed to the free stream wind speed:

$$\lambda = \frac{\Omega R}{U}. \tag{3.21}$$

The relationship between the local tip speed ratio and the TSR is:

$$\lambda_r = \frac{\Omega r}{U} = \frac{\lambda r}{R}. \tag{3.22}$$

[1] Please note that the subscripts to the equation refer to the values of the variable evaluated at the corresponding sections referring to Figure 3.5

Applying the conservation of angular momentum, instead, the expression of the torque on the rotor Q can be obtained. This means that the torque exerted on the rotor must equal the change in angular momentum of the wake:

$$dQ = d\dot{m}(\omega r)r = \rho U_2 2\pi r dr(\omega r)r, \tag{3.23}$$

and since $U_2 = U(1-a)$ and for the definition of angular induction factor of Equation 3.17:

$$dQ = 4a'(1-a)\frac{1}{2}\rho U\Omega r^2 2\pi r dr. \tag{3.24}$$

The power generated at each element is:

$$dP = \Omega dQ, \tag{3.25}$$

thus, substituting Equation 3.24 in this expression and using the definition of the local speed ratio of Equation 3.20:

$$dP = \frac{1}{2}\rho A U^3 \left[\frac{8}{\lambda^2}a'(1-a)\lambda_r^3 d\lambda_r\right]. \tag{3.26}$$

The incremental contribution to the power coefficient from each annular ring is given by:

$$dC_P = \frac{dP}{\frac{1}{2}\rho A U^3}, \tag{3.27}$$

thus

$$C_P = \frac{8}{\lambda^2}\int_0^{\lambda} a'(1-a)\lambda_r^3 d\lambda_r. \tag{3.28}$$

To solve this integral the variables a, a' and λ_r need to be related. This analysis provides the trend of $C_{P,max}$ as a function of the TSR, shown graphically in Figure 3.6. This representation also includes the Betz limit of the ideal turbine obtained in Section 3.1. The higher the TSR, the closer the C_P to the theoretical maximum. Finally, two equations from momentum theory are needed in BEM: the thrust and the torque on an annular cross-section of the rotor. These are respectively determined from Equations 3.19 and 3.24, and are function of the axial and angular induction factor:

$$dT = \rho U^2 4a(1-a)\pi r dr, \tag{3.29}$$

$$dQ = 4a'(1-a)\rho U\pi r^3\Omega dr. \tag{3.30}$$

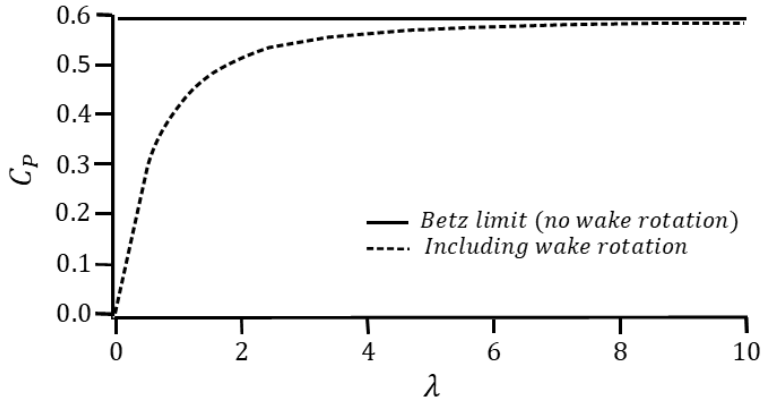

Figure 3.6: Theoretical maximum power coefficient for an ideal HAWT, with and without wake rotation.

3.2.2 Blade element theory

Blade element theory refers to an analysis of forces at a section of the blade, as a function of blade geometry [17]. These forces can also be expressed as a function of lift and drag coefficients and the angle of attack. For this analysis, the blade is divided into N sections (or elements), as shown in Figure 3.7. In addition, two assumptions are made:

- there is no aerodynamic interaction between elements,
- the forces on the blades are determined only by the lift and drag characteristics of the airfoil shape of the blades.

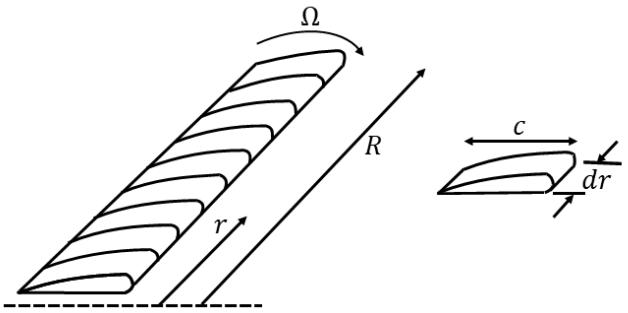

Figure 3.7: Schematic of blade elements (c: airfoil chord length, r: radius, R: rotor radius).

The relative (or effective) wind is the vector sum of the wind velocity at the rotor $U(1-a)$ and the wind velocity due to blade rotation. This second component

is the vector sum of the blade section velocity Ωr, and the induced angular velocity at the blades from the conservation of angular momentum $\omega r/2$:

$$\Omega r + (\omega/2)r = \Omega r + \Omega a' r = \Omega r(1 + a'). \tag{3.31}$$

Figure 3.8 shows the various forces, angles, and velocities at the blade, looking down from the blade tip. The variables are listed below:

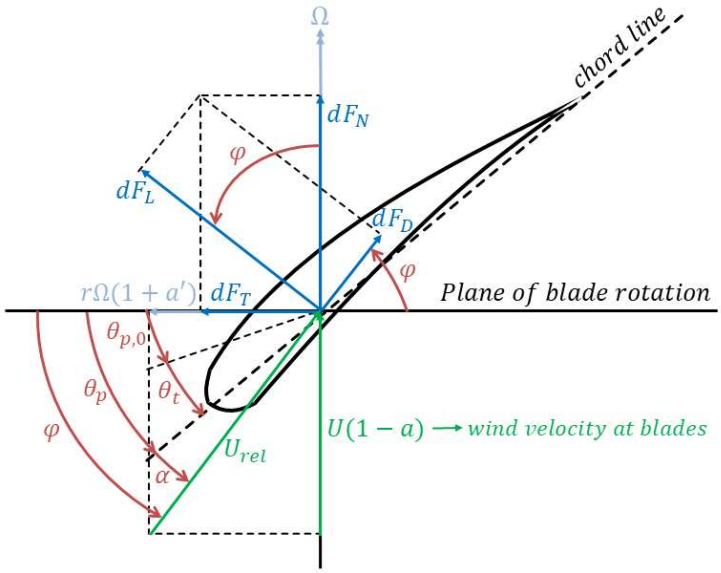

Figure 3.8: Blade geometry analysis of a HAWT.

- θ_p: section pitch angle, which is the angle between the chord line and the plane of rotation;
- $\theta_{p,0}$: blade pitch angle at the tip;
- $\theta_t = \theta_p - \theta_{p,0}$: blade twist angle;
- α: angle of attack (angle between the chord line and the relative wind);
- $\varphi = \theta_p + \alpha$: angle of relative wind;
- dF_L: incremental lift force;
- dF_D: incremental drag force;
- dF_N: incremental force normal to the plane of rotation (it contributes to thrust);

- dF_T: incremental force tangential to the circle swept by the rotor (it creates useful torque);
- U_{rel}: relative wind velocity.

From Figure 3.8 the following relationships can be determined:

$$\tan\varphi = \frac{U(1-a)}{\Omega r(1+a')} = \frac{(1-a)}{(1+a')\lambda_r}, \tag{3.32}$$

$$U_{rel} = \frac{U(1-a)}{\sin\varphi}, \tag{3.33}$$

$$dF_L = C_l \frac{1}{2}\rho U_{rel}^2 c dr, \tag{3.34}$$

$$dF_D = C_d \frac{1}{2}\rho U_{rel}^2 c dr, \tag{3.35}$$

$$dF_N = dF_L \cos\varphi + dF_D \sin\varphi, \tag{3.36}$$

$$dF_T = dF_L \sin\varphi - dF_D \cos\varphi, \tag{3.37}$$

$$dF_N = B\frac{1}{2}\rho U_{rel}^2 (C_l \cos\varphi + C_d \sin\varphi) c dr, \tag{3.38}$$

with C_l lift coefficient, C_d drag coefficient, B number of blades. The differential torque due to the tangential force operating at a distance r from the center is:

$$dQ = B r dF_T, \tag{3.39}$$

so

$$dQ = B\frac{1}{2}\rho U_{rel}^2 (C_l \sin\varphi - C_d \cos\varphi) c r dr. \tag{3.40}$$

Finally, two equations are obtained also from blade element theory: Equation 3.38 and Equation 3.40, that define respectively the normal force (thrust) and the tangential force (torque) on the annular rotor section as function of the flow angles at the blades and airfoil characteristics.

3.2.3 BEM derivation

BEM is finally derived by merging these two theories. This involves combining two equations from momentum theory (Equations 3.29 and 3.30) and two from blade element theory (3.38 and 3.40). The resulting model is capable of both determining the ideal blade shape for optimal rotor performance and evaluating rotor performance for any given blade shape [16]. For a generalized rotor, including wake rotation, by equating the torque equations from momentum and blade element

theory (Equations 3.30 and 3.40), and setting C_d equal to zero (this simplification is commonly accepted, as it introduces negligible errors for airfoils with low drag coefficients), it is obtained:

$$\frac{a'}{(1-a)} = \frac{\sigma' C_l}{4\lambda_r \sin\varphi}, \tag{3.41}$$

where $\sigma' = \frac{Bc}{2\pi r}$ is defined as local solidity. By equating, instead, the normal force equations from the two methods (Equations 3.29 and 3.38), one obtains:

$$\frac{a}{(1-a)} = \frac{\sigma' C_l \cos\varphi}{4\sin^2\varphi}. \tag{3.42}$$

In the end, exploiting Equations 3.32, 3.41 and 3.42, the following useful relationships are obtained:

$$C_l = 4\sin\varphi \frac{\cos\varphi - \lambda_r \sin\varphi}{\sigma'(\sin\varphi + \lambda_r \cos\varphi)}, \tag{3.43}$$

$$\frac{a'}{(1+a')} = \frac{\sigma' C_l}{4\cos\varphi}. \tag{3.44}$$

Other useful expressions include:

$$\frac{a}{a'} = \frac{\lambda_r}{\tan\varphi}, \tag{3.45}$$

$$a = \frac{1}{1 + 4\sin^2\varphi/(\sigma' C_l \cos\varphi)}, \tag{3.46}$$

$$a' = \frac{1}{(4\cos\varphi/(\sigma' C_l)) - 1}. \tag{3.47}$$

Using an iterative method, the unknowns can be determined, allowing for the calculation of the total thrust T and torque Q [18]. Consequently, rotor power can be calculated as:

$$P = \int \Omega dQ = \Omega Q. \tag{3.48}$$

3.3 Classical momentum model limitations

Classical 1D momentum theory is known to fail in the flow conditions typical of modern wind turbines: high-thrust regions and yaw misalignment between the inflow and the rotor.

Wind turbines operate in high-trust regions when their thrust coefficient has a value higher than $C_T \approx 24/25 = 0.96$. This condition often verifies at low wind

speed, specifically in control region 1.5 [2], where the rotor speed and tip-speed ratio are higher than optimal. This is done to limit the rotor speed range and avoid tower resonance. In standard soft-stiff tower designs, control region 1.5 establishes a lower boundary for rotor speed. As a result, at wind speeds below 7-8 m/s, the turbine operates with a tip-speed ratio higher than optimal, leading to thrust coefficient values exceeding the threshold at these wind speeds [20]. Figure 3.9 shows the thrust coefficient as a function of axial induction, highlighting the standard curve from momentum theory and the regions where the theory fails.

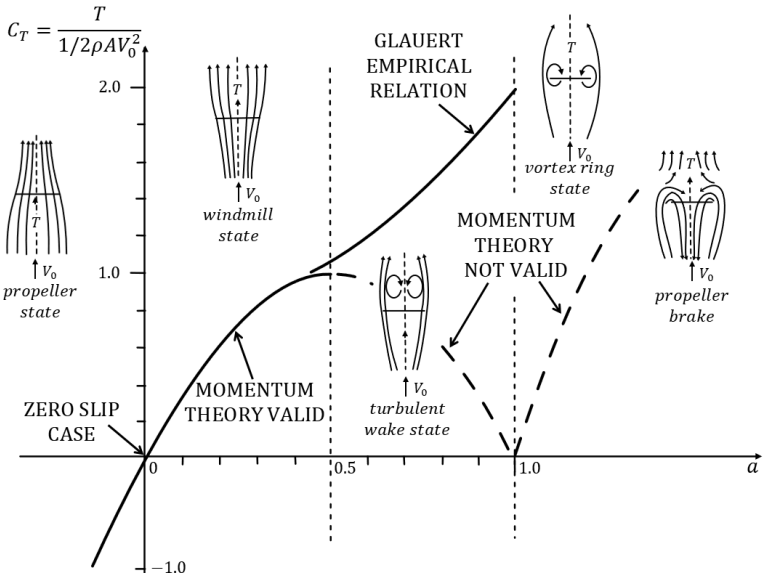

Figure 3.9: Thrust coefficient as a function of axial induction.

Concerning yaw misalignment, instead, wind turbines are always subject to some level of misalignment with the incoming wind direction, largely due to the slow response of the yaw controller and inaccuracies or biases in wind direction measurements [21]. These misalignment errors tend to be more pronounced in FOWTs) [22]. Additionally, yaw misalignment can now be intentional, as seen in wake steering, a control strategy used to mitigate the negative impact of a wind turbine's wake on the performance of neighboring turbines [23].

This theory breakdown results in significant errors in rotor thrust, power, wake velocities, and outlet pressure estimations [6]. Classical momentum modeling, in fact, predicts a decrease in thrust as the induction increases after the threshold value, while experiments and CFD simulations demonstrate the opposite trend.

[2] A transitional region of the power curve where the turbine spins at low wind speeds without generating power [19]

Due to these limitations, current predictions of wind turbine forces and power output often utilize empirical formulas to correct the classical monodimensional momentum theory, which will be explained in detail later in this chapter. The shortcomings of classical momentum theory result from two primary assumptions: wake pressure recovery to match the freestream value and one-dimensional flow perpendicular to the rotor [6]. The first hypothesis is not respected at higher thrust coefficients where the static pressure in the wake downstream of the rotor fails to return to the freestream pressure. This persistent pressure drop behind the rotor, known as base suction, corresponds to an additional thrust force contribution that classical models do not capture [6]. The second assumption, instead, implies neglecting all the lateral velocities induced by the rotor misalignment.

3.4 Empirical corrections

Classical aerodynamic models rely on empirical corrections to address operational regimes where the theory fails, such as high-thrust regions and yaw misalignment inflows. These corrections modify the basic assumptions of momentum theory to account for real-world phenomena that the idealized models do not capture.

This section focuses on two of the most widely used corrections in the literature, each addressing a specific issue: the Glauert correction for high-thrust conditions and the skewed wake correction for rotor misalignment.

3.4.1 Glauert correction

Glauert correction (1926) is used to model high-thrust operations. His model was based on experimental measurements of helicopter rotors with large induced velocities, but it can also be used, in combination with the tip-loss model [16, 17], on individual blade elements within the BEM theory. According to Glauert, when the axial induction factor exceeds approximately $a = 1/3$, the thrust coefficient can no longer be accurately calculated using Equation 3.15. Instead, a more appropriate expression is given by:

$$C_T = 4a\left[1 - \frac{1}{4}(5 - 3a)a\right]. \tag{3.49}$$

3.4.2 Skewed wake correction

To represent the effect of rotor misalignment, 1D momentum theory is typically adjusted using empirical skewed wake corrections. Skewed wakes refer to wakes that are not symmetric with the turbine axis [16]. The original correction formulation to model the effects of a skewed wake, developed by Glauert, applies a multiplicative

correction factor to the axial induction factor that is a function of wake skew angle χ (through K), radial position, and blade azimuth angle ψ::

$$a_{skew} = a\left(1 + K\frac{r}{R}\cos\psi\right). \tag{3.50}$$

Among the correction models derived from this formula, one commonly used approach is the Pitt and Peters model (1981):

$$a_{skew} = a\left(1 + \frac{15\pi}{32}\frac{r}{R}\tan\frac{\chi}{2}\cos\psi\right). \tag{3.51}$$

All the relevant angles are shown in Figure 3.10. The wake angle is the actual flow angle at which the flow leaves the turbine and is slightly larger than the skew angle, which is the difference between the incoming flow direction and the rotor plane. An approximated formula to relate the wake skew angle χ to the yaw angle γ is:

$$\chi = (0.6a + 1)\gamma. \tag{3.52}$$

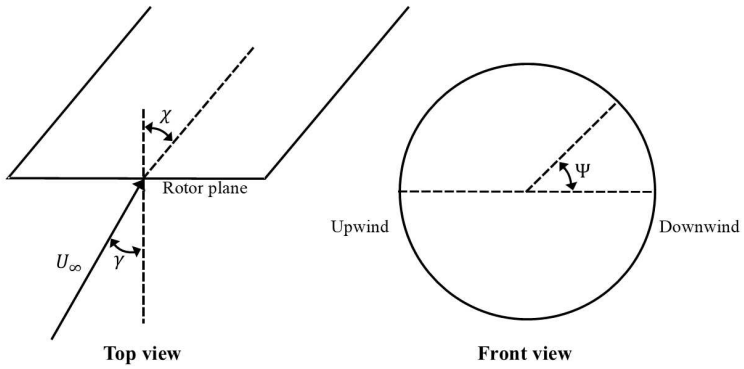

Figure 3.10: Coordinates used in skewed wake correction.

The major limitation of this model is that it assumes a cylindrical wake, which is valid only for lightly loaded rotors [17].

3.4.3 Other corrections

In addition to the well-known corrections discussed so far, numerous other attempts have been proposed within the research landscape. Some examples include: a new formulation of the thrust coefficient to resolve the discontinuity between the thrust coefficient and axial induction when tip losses are considered [24]; a comparison of various break state models to determine which is most suitable for the wind turbine model being simulated [18]; and a power-yaw formula to account for rotor misalignment [22, 25].

3.5 Beyond classical models

This gap in theoretical modeling has only recently been addressed more definitively by the research titled *"Unified Momentum Model for Rotor Aerodynamics Across Operating Regimes"* [6]. This study introduces a novel model for complex turbine aerodynamics that, coupled with blade element modeling, leads to a new unified BEM approach able to predict power production, thrust force and wake dynamics across all operating regimes, without the need for empirical corrections. The UMM marks a significant advancement in rotor modeling since, besides CFD simulations, it is the only first principles theory able to accurately predict rotor aerodynamics at arbitrary thrust forces and misalignment conditions. Furthermore, UMM provides a simple model that could find an application in high-throughput optimization, unlike CFD simulations, whose computationally intense nature limits their use in optimization processes [6]. The details of the UMM will be thoroughly explained in the following chapter.

Chapter 4

Unified momentum model

The UMM, developed by J. Liew et al. at the Massachusetts Institute of Technology (MIT) and published in August 2024 in the research article *"Unified Momentum Model for Rotor Aerodynamics Across Operating Regimes"* [6], represents a significant advancement in rotor aerodynamics. This model generalizes and replaces the classical momentum theory 3.1 and is designed to integrate seamlessly within the BEM framework for turbine rotor predictions. Unlike its predecessors, the UMM can accurately predict rotor aerodynamics across all operating regimes, including scenarios with arbitrary inflow angles and high thrust coefficients, without relying on empirical corrections that were essential in traditional aerodynamic models. This eliminates a major limitation of classical approaches and enhances the model's applicability in the aerodynamic conditions where modern wind turbines often operate.

The UMM is structured around five governing equations that describe rotor induction, thrust, wake velocities, wake pressure, and power production. Together, these equations provide a comprehensive and unified approach to modeling rotor aerodynamics.

This chapter outlines the fundamental principles and equations of the UMM, setting the stage for its application and analysis in subsequent sections.

4.1 Fundamentals of the UMM

This model overcomes traditional momentum theory limitations by:

- incorporating the pressure deficit in the rotor wake, using a solution to the differential Euler equations,
- accounting for rotor misalignment through a lifting line model.

Consequently, UMM can predict the empirically observed monotonic increase in thrust coefficient, depicted in Figure 4.1, which classical momentum theory fails to reproduce beyond a certain axial induction factor.

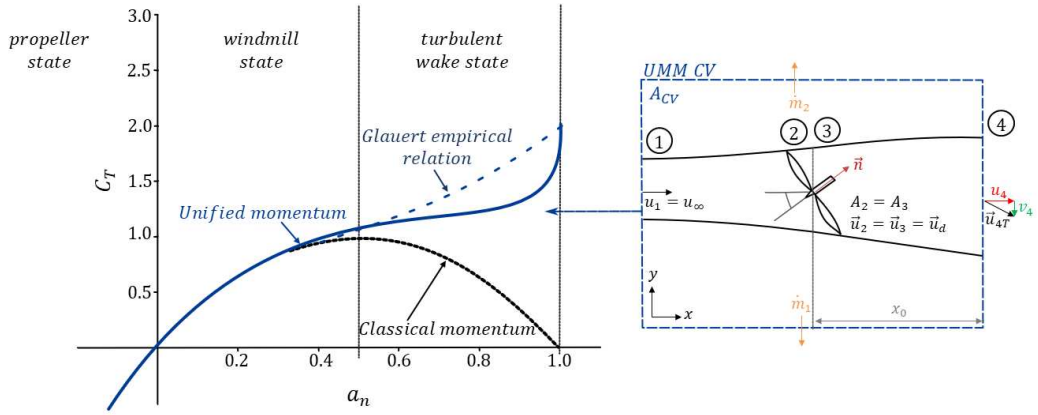

Figure 4.1: Thrust coefficient variations with induction factor using classical one-dimensional momentum model, Glauert's empirical relation, and the UMM. Representation of the control volume used to derive the UMM.

As for classical theory, the model is derived under uniform, inviscid inflow and neglects turbulence. Therefore, the model can be applied at the rotor, and in the near-wake, which is the portion of wake before turbulent mixing.

4.2 Model derivation and principles

The five analytical equations are obtained from the analysis of the control volume shown in Figure 4.1, using conservation of mass, momentum, and energy. This section will outline the derivation of each equation governing the UMM.

The model is based on the following primary inputs:

- The modified thrust coefficient C'_T,
- The yaw angle γ.

4.2.1 Thrust force

The modified thrust coefficient controls the thrust force that is defined as [26]:

$$\vec{F_T} = -\frac{1}{2}\rho C'_T A_d (\vec{u_d} \cdot \hat{n})^2 \hat{n}, \tag{4.1}$$

where $\vec{u_d}$ is the velocity at the actuator disk, A_d is the disk area, and $\hat{n}$ is the unit vector normal to the disk. The system of equations considers both yaw-aligned

and yaw-misaligned actuator disks. The rotor-normal induction factor a_n, which measures the degree of velocity reduction as the wind passes through the rotor plane, is defined as:

$$a_n = 1 - \frac{\vec{u_d} \cdot \vec{n}}{u_\infty cos(\gamma)}, \tag{4.2}$$

and it is the generalization, to account for yaw misalignment, of the standard (axial) induction factor a used in classical one-dimensional momentum theory, derived from Equation 3.1. For the yaw-aligned case, indeed, a_n reduces to a. The thrust force can thus be expressed as a function of the rotor-normal induction factor a_n and the yaw angle as:

$$\vec{F_T} = -\frac{1}{2}\rho C'_T A_d (1 - a_n)^2 cos^2(\gamma) u_\infty^2 [cos(\gamma)\hat{i} + sin(\gamma)\hat{j}]. \tag{4.3}$$

The power for the actuator disk is:

$$P = -\vec{F_T} \cdot \vec{u_d}. \tag{4.4}$$

4.2.2 Bernoulli equation

This analysis is similar to classical momentum theory, with the exception that in this case the wake pressure p_4 is not assumed equal to the rotor pressure p_1. The velocity is continuous over the porous actuator disk, therefore $\vec{u_2} = \vec{u_3}$. The pressure just upwind of the porous disk is:

$$p_2 = p_1 + \frac{1}{2}\rho(||\vec{u_1}||^2 - ||\vec{u_2}||^2), \tag{4.5}$$

and the pressure just downwind of the porous disk is:

$$p_3 = p_4 + \frac{1}{2}\rho(||\vec{u_4}||^2 - ||\vec{u_2}||^2), \tag{4.6}$$

where, at a given yaw angle, $||\vec{u_4}||$ has two components: the streamwise wake velocity u_4, and the lateral wake velocity v_4. Combining Equations 4.5 and 4.6:

$$p_4 - p_1 = \frac{1}{2}\rho(||\vec{u_1}||^2 - ||\vec{u_4}||^2) + \frac{||\vec{F_T}||}{A_d}, \tag{4.7}$$

where $\frac{\vec{F_T}}{A_d} = -\frac{1}{2}\rho C'_T (1 - a_n)^2 cos^2(\gamma) u_\infty^2$. Substituting this expression yields:

$$p_4 - p_1 = \frac{1}{2}\rho(||\vec{u_1}||^2 - ||\vec{u_4}||^2) - \frac{1}{2}\rho C'_T (1 - a_n)^2 cos^2(\gamma) u_\infty^2. \tag{4.8}$$

Lastly, solving for the rotor-normal induction gives the first equation of the UMM system:

$$a_n = 1 - \sqrt{\frac{u_\infty^2 - u_4^2 - v_4^2}{C'_T cos^2(\gamma) u_\infty^2} - \frac{p_4 - p_1}{\frac{1}{2}\rho C'_T cos^2(\gamma) u_\infty^2}}. \tag{4.9}$$

4.2.3 Streamwise momentum balance

The streamwise velocity is derived from the momentum conservation in the streamwise direction, assuming uniform flow within the stream tube:

$$\vec{F_T} \cdot \hat{i} = \rho u_4^2 A_4 - \rho u_\infty^2 A_4 + \dot{m}_{out} u_\infty + A_4(p_4 - p_1), \tag{4.10}$$

where $\dot{m}_{out} = \dot{m}_1 + \dot{m}_2$ is the mass flux out of the top and bottom of the control volume. For the uniform flow assumption, the streamwise velocity and pressure on the downstream cylinder cross-sectional area are u_1 and p_1, respectively, except in the A_4 region, where they are u_4 and p_4. For the mass conservation in the stream tube:

$$A_4 = \frac{(1 - a_n)cos(\gamma)A_d u_\infty}{u_4}. \tag{4.11}$$

From mass conservation in the control volume, the mass flux out of the control volume is:

$$\dot{m}_{out} = \rho A_4(u_\infty - u_4). \tag{4.12}$$

Combining Equations 4.10, 4.11 and 4.12:

$$\vec{F_T} \cdot \hat{i} = \rho(1 - a_n)\frac{u_\infty}{u_4}cos(\gamma)A_d(u_4^2 - u_\infty) + \frac{(1 - a_n)cos(\gamma)A_d u_\infty}{u_4}(p_4 - p_1). \tag{4.13}$$

The final equation for u_4 is:

$$u_4^2 + \left(\frac{1}{2}C_T'(1 - a_n)cos^2(\gamma)u_\infty - u_\infty\right)u_4 + \frac{1}{\rho}(p_4 - p_1) = 0, \tag{4.14}$$

that solved using the quadratic formula gives the second equation of the UMM:

$$u_4 = -\tfrac{1}{4}C_T'(1 - a_n)\cos^2(\gamma)u_\infty + \tfrac{u_\infty}{2} + \tfrac{1}{2}\sqrt{\left(\tfrac{1}{2}C_T'(1 - a_n)\cos^2(\gamma)u_\infty - u_\infty\right)^2 - \tfrac{4(p_4 - p_1)}{\rho}} \tag{4.15}$$

4.2.4 Lifting line model for the lateral wake velocity

The lateral wake velocity v_4 is modeled using Prandtl's lifting line theory [27], accounting for the yaw misalignment through the elliptical lift distribution. An elliptic lift distribution results in a constant downwash (lateral velocity). The circulation at the disk hub height ($z = 0$) is defined as:

$$\Gamma_0 = -\frac{2F_L}{\rho\pi R u_\infty}, \tag{4.16}$$

where the F_L is the total lift force $L = -\vec{F_T} \cdot \hat{j}$ and R is the disk radius. From [27], the lateral velocity disturbance is thus:

$$\delta v_0 = v_\infty - v_4 = \frac{-\Gamma_0}{4R} = \frac{-\vec{F_T} \cdot \hat{j}}{2\rho u_\infty A_d} = \frac{1}{4} C'_T u_\infty sin(\gamma) cos^2(\gamma)(1 - a_n(\gamma))^2, \quad (4.17)$$

and since $v_\infty = 0$ as the freestream flow is only in the streamwise direction, the third equation of the model is obtained:

$$v_4 = -\frac{1}{4} C'_T (1 - a_n)^2 sin(\gamma) cos^2(\gamma) u_\infty. \quad (4.18)$$

4.2.5 Near-wake length

The near-wake length x_0 is the distance from the rotor to the point where turbulent mixing begins in the wake. This parameter is key in determining the pressure drop over the control volume $p_4 - p_1$, as the streamwise location of the boundary of the control volume must be known. Following the approach proposed by [28], the differential form of the shear layer width s is:

$$\left| \frac{u_s}{u_\infty} \right| \frac{ds}{dx} = \beta \left| \frac{u_e}{u_\infty} \right|, \quad (4.19)$$

where $u_s = (u_\infty + u_4)/2$ is the characteristic shear layer velocity, $u_e = (u_\infty - u_4)/2$ is the characteristic relative velocity, and β is the wake or jet spread rate. The last parameter is unknown, thus a value of $\beta = 0.1403$ is chosen, which is in the standard range found in the literature. The shear layer thickness at $x = x_0$ is:

$$\frac{s}{D} = \frac{cos(\gamma)}{2} \sqrt{\frac{u_2}{u_\infty + u_4}}, \quad (4.20)$$

where D is the actuator disk diameter and $u_2 = (1 - a_n) cos(\gamma) u_\infty$ is the streamwise velocity at the disk. Integrating both sides results in the fourth equation of the UMM, which is expressed as:

$$\frac{x_0}{D} = \frac{cos(\gamma)}{2\beta} \frac{u_\infty + u_4}{|u_\infty - u_4|} \sqrt{\frac{(1 - a_n) cos(\gamma) u_\infty}{u_\infty + u_4}}. \quad (4.21)$$

4.2.6 Outlet pressure modeling

The pressure model is based on the solution to the steady, two-dimensional Euler equations with an actuator disk turbine [29] [30]. The wake pressure drop is decomposed in a linear component p^L and a non-linear component p^{NL}: the pressure contribution from rotor body forces, and the pressure contribution from

flow advection, respectively. The linear component can be easily solved analytically, while the non-linear term has no closed-form solution. The sequence of mathematical steps contained in this section refers to the "*Supplementary Information*" document of [6]. The Euler equations with constant density ρ are:

$$u_j \frac{\partial u_i}{\partial x_j} = -\frac{1}{\rho}\frac{\partial p}{\partial x_i} + f_i, \tag{4.22}$$

where f_i is the actuator disk body forcing in the i^{th} direction. The mass conservation is given by $\partial u_i/\partial x_j = 0$ and, since the velocity field is decomposed into the background flow $u = u_\infty + w_x$ and actuator disk-induced component $v = w_y$ (there is no freestream flow in the lateral directions), it can be reduced to $\partial w_x/\partial x + \partial w_y/\partial y = 0$. The resulting momentum equations for the induced velocities w_x and w_y with constant density ρ are:

$$u_\infty \frac{\partial w_x}{\partial x} = -\frac{1}{\rho}\frac{\partial p}{\partial x} + f_x - \left(w_x \frac{\partial w_x}{\partial x} + w_y \frac{\partial w_x}{\partial y} \right), \tag{4.23}$$

$$u_\infty \frac{\partial w_y}{\partial x} = -\frac{1}{\rho}\frac{\partial p}{\partial y} + f_y - \left(w_x \frac{\partial w_y}{\partial x} + w_y \frac{\partial w_y}{\partial y} \right), \tag{4.24}$$

where f_x and f_y represent the actuator disk body forcing. Using the divergence-free velocity condition for the pressure, the conservation of mass becomes:

$$\frac{\partial^2 p}{\partial x^2} + \frac{\partial^2 p}{\partial y^2} = \rho\left(\frac{\partial f_x}{\partial x} + \frac{\partial f_y}{\partial y} \right) + \rho\left(\frac{\partial g_x}{\partial x} + \frac{\partial g_y}{\partial y} \right), \tag{4.25}$$

where g_x and g_y are the nonlinear force field due to advection. They are equal to:

$$g_x = -\left(w_x \frac{\partial w_x}{\partial x} + w_y \frac{\partial w_x}{\partial y} \right), \tag{4.26}$$

$$g_y = -\left(w_x \frac{\partial w_y}{\partial x} + w_y \frac{\partial w_y}{\partial y} \right). \tag{4.27}$$

In two-dimensional space, the pressure field around an actuator line that is nearly infinitesimally thin and uniformly loaded, assuming an inviscid (Euler) flow, can be described as a combination of two components: $p(x, y) = p^L(x, y) + p^{NL}(x, y)$. For the linearity of the Poisson equation 4.25, these pressure contributions are:

$$\frac{\partial^2 p^L}{\partial x^2} + \frac{\partial^2 p^L}{\partial y^2} = \rho\left(\frac{\partial f_x}{\partial x} + \frac{\partial f_y}{\partial y} \right), \tag{4.28}$$

$$\frac{\partial^2 p^{NL}}{\partial x^2} + \frac{\partial^2 p^{NL}}{\partial y^2} = \rho\left(\frac{\partial g_x}{\partial x} + \frac{\partial g_y}{\partial y} \right). \tag{4.29}$$

The streamwise and lateral velocity deviations from the mean, w_x and w_y can also be decomposed into a linear and nonlinear component:

$$w_x = w_x^L + w_x^{NL}, \tag{4.30}$$

$$w_y = w_y^L + w_y^{NL}. \tag{4.31}$$

From the two-dimensional Euler equations (Equations 4.23 and 4.24) the momentum equations for the linear induced velocities thus become:

$$u_\infty \frac{\partial w_x^L}{\partial x} = -\frac{1}{\rho}\frac{\partial p^L}{\partial x} + f_x, \tag{4.32}$$

$$u_\infty \frac{\partial w_y^L}{\partial x} = -\frac{1}{\rho}\frac{\partial p^L}{\partial y} + f_y. \tag{4.33}$$

The analytical solution for the linear pressure component p_L is:

$$p^L(x,y) = -\frac{\Delta p}{2\pi}\left(\arctan\left(\frac{D+2y}{2x}\right) + \arctan\left(\frac{D-2y}{2x}\right)\right), \tag{4.34}$$

where $\Delta p = p_2 - p_3 = -||\vec{F_T}||/A_d = \frac{1}{2}\rho C_T'(1-a_n)^2\cos^2(\gamma)u_\infty^2$ is the pressure drop over the rotor, and x and y are normalized by the rotor diameter. Therefore, the centerline pressure at the near-wake length ($x = x_0$, $y = 0$) can be expressed as:

$$\begin{aligned} p_4 - p_1 &= p^L(x = x_0, y = 0) + p^{NL}(x = x_0, y = 0) = \\ &= -\frac{1}{2\pi}\rho C_T'(1-a_n)^2\cos^2(\gamma)u_\infty^2 \arctan\left[\frac{1}{2}\frac{D}{x_0}\right] + p^{NL}(x = x_0, y = 0). \end{aligned} \tag{4.35}$$

Being the nonlinear pressure term function of C_T', γ, a_n and x_0, the fifth equation of the UMM model is finally expressed as:

$$p_4 - p_1 = -\frac{1}{2\pi}\rho C_T'(1-a_n)^2 cos^2(\gamma)u_\infty^2 arctan\left[\frac{1}{2}\frac{D}{x_0}\right] + p^{NL}(C_T', \gamma, a_n, x_0). \tag{4.36}$$

The analytical solution for the linear components w_x and w_y is:

$$w_x^L(x,y) = \frac{\Delta p}{2\pi\rho u_\infty}\left(\arctan\left(\frac{D+2y}{2x}\right) + \arctan\left(\frac{D-2y}{2x}\right)\right) - \Delta p/(\rho u_\infty), \tag{4.37}$$

$$w_y^L(x,y) = \frac{\Delta p}{4\pi\rho u_\infty}\ln\left(\frac{4x^2 + (2y+D)^2}{4x^2 + (2y-D)^2}\right), \tag{4.38}$$

with the presence of the term $\Delta p/(\rho u_\infty)$ of Equation 4.37 only when behind the rotor, so for $x > 0$ and $|y| < D/2$. Concerning the nonlinear pressure p^{NL}, the presence of advection does not permit an analytical solution. The momentum equations for the nonlinear induced velocities are:

$$u_\infty \frac{\partial w_x^{NL}}{\partial x} = -\frac{1}{\rho}\frac{\partial p^{NL}}{\partial x} + g_x, \tag{4.39}$$

$$u_\infty \frac{\partial w_y^{NL}}{\partial x} = -\frac{1}{\rho}\frac{\partial p^{NL}}{\partial y} + g_y. \tag{4.40}$$

The nonlinear pressure contribution in Equation 4.29 depends on the nonlinear terms g_x and g_y which depend on the full induced velocities w_x and w_y that, according to Equations 4.30 and 4.31, have both linear and nonlinear components. Thus, the pressure-Poisson equation 4.29 is solved using a Green's function approach, giving a solution of the form:

$$p^{NL}(x,y) = \frac{\rho}{2\pi}\iint_{\mathbb{R}^2} \frac{g_x(x-x') + g_y(y-y')}{(x-x')^2 + (y-y')^2}\, dx'\, dy', \tag{4.41}$$

that can be expressed as the sum of two convolutions:

$$p^{NL}(x,y) = \frac{\rho}{2\pi}\left(g_x * \frac{x}{x^2+y^2} + g_y * \frac{y}{x^2+y^2}\right). \tag{4.42}$$

The nonlinear velocity components are obtained, from Equations 4.39 and 4.40, as:

$$w_x^{NL}(x,y) = \frac{-p^{NL}}{\rho u_\infty} + \int_{-\infty}^{x} \frac{g_x}{u_\infty} dx', \tag{4.43}$$

$$w_y^{NL}(x,y) = \int_{-\infty}^{x} \left(-\frac{1}{\rho u_\infty}\frac{\partial p^{NL}}{\partial y} + \frac{g_y}{u_\infty}\right) dx'. \tag{4.44}$$

The non-linear pressure system is solved iteratively, as described in Section 4.3.1. As shown in Figure 4.2, the non-linear pressure contribution is negligible for low values of rotor thrust ($\Delta p/\rho u_\infty^2 \lesssim 0.4$ or $C_T \lesssim 0.8$), whilst it becomes influential in the high-thrust states, and even more significant further downstream ($x \gtrsim D$) due to base suction. Neglecting p_{NL} makes the system of equations completely analytical, but it results in an underestimation of the pressure drop, therefore causing under-predictions of u_4, C_P, and C_T, as shown in Figure 4.3. If, contrarily, the non-linear pressure term is included, the UMM shows excellent results in all operating regions.

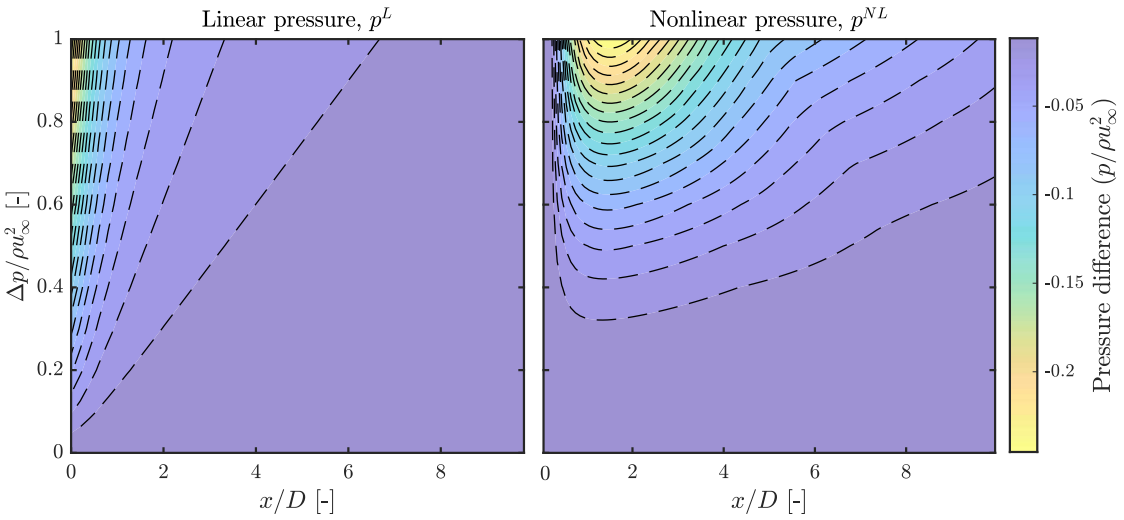

Figure 4.2: Centerline pressure behind the actuator disk as a function of downstream distance x/D, and disk pressure drop Δp.

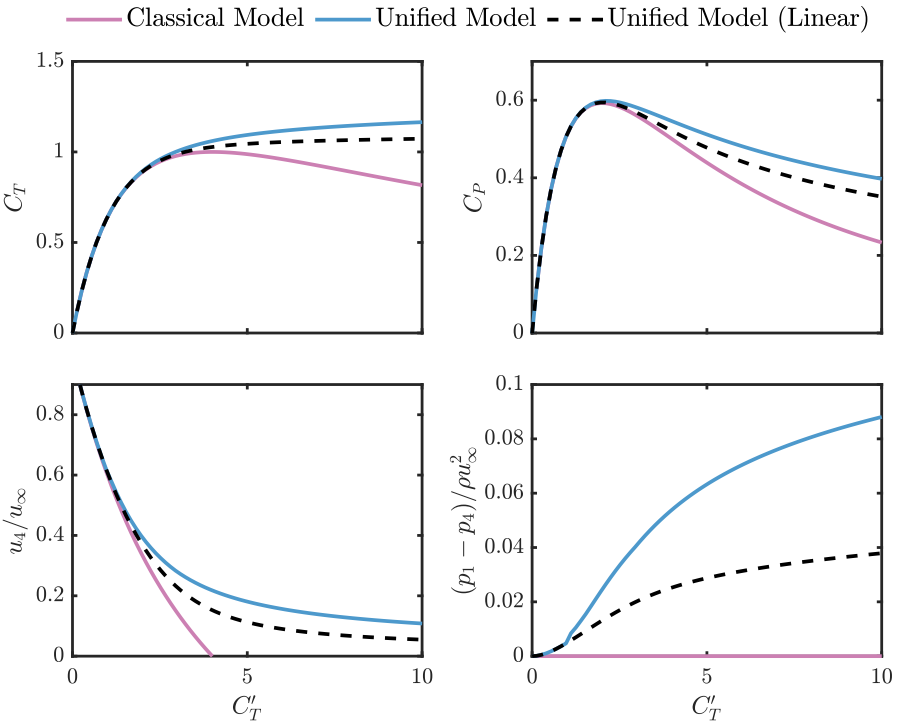

Figure 4.3: Thrust coefficient C_T, power coefficient C_P, streamwise wake velocity u_4, density-normalized wake pressure deficit $p_1 - p_4$ as a function of the local thrust coefficient C_T'.

4.2.7 System of equations

The final form of the five equations, with *rotor-normal induction a_n, streamwise wake velocity u_4, lateral wake velocity v_4, near-wake length x_0, and pressure drop in the wake $p_4 - p_1$* as outputs, consists of Equations 4.9, 4.15, 4.18, 4.21, and 4.36. A more accurate prediction of wake dynamics, compared to classical models, achieved through Equations 4.15, 4.18, and 4.21, is crucial for reliably modeling downstream effects in wind farms, where wake interactions significantly influence energy capture and turbine performance. Equation 4.36 is essential to understanding the increase in thrust force at high induction levels.

4.2.8 Variation with C_T as input

In some applications, for instance for blade-element modeling of a rotor or when the thrust curve of a utility-scale wind turbine is available as a function of the freestream wind speed, it is far more convenient to utilize as input the thrust coefficient C_T rather than the local one C'_T. However, to obtain a mathematically and physically equivalent model, this choice results in the need for a sixth equation that expresses the thrust coefficient as a function of the induction and the yaw misalignment angle:

$$C'_T = \frac{C_T}{(1-a_n)^2 cos^2(\gamma)}. \tag{4.45}$$

The thrust coefficient is defined as:

$$C_T = \frac{2||\vec{F_T}||}{\rho A_d u_\infty^2}, \tag{4.46}$$

where $||\vec{F_T}||$ is the magnitude of the thrust force.

4.3 Solution method

The system of equations is solved using a fixed-point iteration, where an initial guess is provided for each variable $\mathbf{x^{(0)}} = [a_N^{(0)}, u_4^{(0)}, v_4^{(0)}, x_0^{(0)}, (p_4 - p_1)^{(0)}]^T$ (with the addition of $C'^{(0)}_T$ if C_T is used as input) and iterated until convergence is reached with the desired tolerance ϵ. The iterations proceed as:

$$\mathbf{x}^{(k+1)} = \mathbf{x}^{(k)} + (1-\omega)\mathbf{r}(\mathbf{x}^{(k)}), \tag{4.47}$$

where $\mathbf{r(x)}$ are residual equations from the system of equations, and ω is a relaxation parameter, comprised between 0 and 1, which improves numerical stability. Convergence is reached when $||\mathbf{r}(\mathbf{x^{(k)}})||_\infty < \epsilon$.

4.3.1 Nonlinear pressure field solution

The calculation of the centerline pressure behind the actuator disk requires an iterative solution to a two-dimensional pressure field. The iterative process involves Equations 4.29, and 4.39-4.44. The initial conditions for the iteration are: $w_x^{NL}(x,y) = w_y^{NL}(x,y) = 0$ and $p^{NL}(x,y) = 0$. Then, the procedure consists of three main steps:

- Computation of the nonlinear forcing terms, g_x and g_y, as defined in Equations 4.26 and 4.27, using the velocity components from Equations 4.30 and 4.31;
- Computation of Equation 4.42 to determine the nonlinear pressure term p^{NL}, performing the convolution in Fourier space;
- Update of the nonlinear induced velocities w_x^{NL} and w_y^{NL}, through Equations 4.43 and 4.44, respectively.

These steps are iterated until the centerline pressure field is resolved. To reduce computational time, the nonlinear centerline pressure can be tabulated as a function of $\Delta p/(\rho u_\infty^2) \in [-1,1]$ and $x \in [0, \sim 20D]$ (a graphical representation is shown on the right side of Figure 4.2), and used as a lookup table during runtime evaluation of the UMM equations. It has to be noted that the pressure formulation presents some numerical instability, with the issue of numerical divergence particularly evident at higher thrust coefficients, where iterative solvers often fail to converge. This challenge is addressed by monitoring minimum pressure values along the centerline, which serves as an approximate upper bound for the nonlinear pressure drop, though further analysis is warranted to fully understand and resolve the instability [6].

4.4 Performance of the UMM

One of the key advantages of the UMM is its ability to predict the occurrence of the maximum power coefficient of 0.5984 at an induction factor of 0.345, which is slightly higher (by approximately 1-3.5%) than the classical Betz limit (see Section 3.1) [6]. This enhancement arises from the model's ability to account for the wake pressure deficit, an aspect that classical momentum theory ignores, leading to underpredictions of the energy extraction potential in high-trust regimes. Furthermore, the model has also been tested under Atmospheric Boundary Layer (ABL) conditions, where it demonstrated a significant reduction in prediction error, compared to classical momentum theory, for critical parameters [6]:

- Induction: 60% error reduction,
- Streamwise wake velocity: 83% error reduction,

- Spanwise wake velocity: 78% error reduction.

These improvements highlight the robustness of the UMM in a variety of operational conditions.

4.5 A BEM model based on the UMM

Building on the UMM, a BEM model can be constructed. This unified BEM model integrates blade element theory, detailed in Section 3.2.2, with the UMM (system of five equations plus Equation 4.45), which replaces classical momentum theory. As a result, the model can predict the power coefficient across a variety of blade pitch angles and tip-speed ratios, key for determining optimal control strategies. For instance, when simulating yaw-misaligned turbines, the unified BEM model predicts that an optimal strategy would involve reducing blade pitch angles to increase thrust, rather than simply lowering the TSR as classical models suggest. This insight aligns with recent studies that emphasize increasing thrust as an effective strategy in yaw misalignment conditions to maximize power output [31] [32]. Building on this robust foundation, the unified BEM model can be further developed to address more complex operational conditions, such as turbulent and non-uniform inflow, and floating offshore turbines affected by rotational and unsteady motion, as a more reliable alternative to empirical models that could lead to inaccuracies when applied beyond the initial conditions [6].

4.5.1 Unified BEM derivation

The model derivation follows the procedure detailed in the "Supplementary Information" document of [6].

Input variables and geometry

A polar grid (μ, ψ) is defined across the rotor disc to capture azimuthal variations due to yaw misalignment. $\mu \in [0,1] = r/R$ is the radial position normalized by rotor radius R, and ψ is the azimuthal angle. Turbine control settings are introduced as input variables, such as the yaw angle, blade pitch angle, and TSR. Rotor properties, such as airfoil lift and drag coefficients $C_l(\mu, \alpha)$ and $C_d(\mu, \alpha)$, blade solidity $\sigma(\mu)$ and blade twist angle $\theta_t(\mu)$ are known.

Blade forces

The axial velocity v_x and the tangential velocity v_t at each blade sector are determined considering the yaw misalignment and the azimuthal position and are

expressed as:

$$v_x(\mu,\psi) = u_\infty(1-a_n)cos(\gamma), \tag{4.48}$$

$$v_t(\mu,\psi) = (1+a')\lambda\mu - u_\infty(1-a_n)sin(\gamma)cos(\psi). \tag{4.49}$$

The inflow angle ϕ and inflow velocity w are given by:

$$\phi(\mu,\psi) = \arctan(v_x/v_t), \tag{4.50}$$

$$w(\mu,\psi) = \sqrt{v_x^2+v_t^2}. \tag{4.51}$$

The angle of attack α is:

$$\alpha(\mu,\psi) = \phi(\mu,\psi) - \theta_t(\mu) - \theta_p. \tag{4.52}$$

The rotor normal and tangential force coefficients are:

$$C_n(\mu,\psi) = cos(\phi)C_l(\mu,\alpha(\mu,\psi)) + sin(\phi)C_d((\mu,\alpha(\mu,\psi))), \tag{4.53}$$

$$C_{tan}(\mu,\psi) = sin(\phi)C_l(\mu,\alpha(\mu,\psi)) - cos(\phi)C_d((\mu,\alpha(\mu,\psi))), \tag{4.54}$$

Thrust and torque balance

As in classical BEM theory, thrust and torque from momentum balance are equated to the forces calculated from the blade element theory. These forces are computed for each annular segment by averaging over the azimuthal variations. The incremental thrust force, δT, over a radial segment, δr, is equated between the two methods as:

$$\delta T(\mu,\psi) = \frac{1}{2}\rho\omega(\mu,\psi)^2 Bc(\mu)C_n(\mu,\psi)\delta r = \frac{1}{2}\rho C_T(\mu,\psi)u_\infty^2 2\pi r\delta r. \tag{4.55}$$

The thrust coefficient for the annular section is then obtained:

$$C_T(\mu) = \frac{\sigma(\mu)}{2\pi}\int_0^{2\pi}\frac{\omega(\mu,\psi)^2}{u_\infty^2}C_n(\mu,\psi)d\psi, \tag{4.56}$$

and C_T' can be derived through Equation 4.45. C_T' relates to a_n as follows: $a_n(\mu) = g((\frac{C_T'(\mu)}{F(\mu)}),\gamma)$, where $g(C_T',\gamma)$ is the converged solution of the five-equation system, solved iteratively, and $F(\mu)$ is the tip-loss correction factor for the blade element model [6]. Similarly, by equating the incremental torque between theories and incorporating the tip-loss correction, the expression for $a'(\mu)$ is obtained:

$$\delta Q = \rho U_\infty F(\mu)(1-a_n(\mu))\cos(\gamma)2\pi r 2a'(\mu)r^2\Omega\delta r = \tfrac{1}{2}\rho w(\mu,\psi)^2 Bc(\mu,\psi)rC_{\tan}(\mu,\psi)\delta r \tag{4.57}$$

$$a'(\mu) = \frac{\sigma(\mu)}{8\pi F(\mu)\mu^2\lambda(1-a_n(\mu))\cos(\gamma)}\int_0^{2\pi}\frac{w(\mu,\psi)^2}{u_\infty^2}C_{\tan}(\mu,\psi)d\psi. \tag{4.58}$$

Thus, the two equations that close the BEM loop are:

$$a_n(\mu) = g\left(\frac{C'_T(\mu)}{F(\mu)}, \gamma\right), \tag{4.59}$$

$$a'(\mu) = \frac{\sigma(\mu)}{8\pi F(\mu)\mu^2\lambda(1-a_n(\mu))\cos(\gamma)} \int_0^{2\pi} \frac{w(\mu,\psi)^2}{u_\infty^2} C_{\tan}(\mu,\psi)d\psi. \tag{4.60}$$

These two induction factor equations can be solved independently at each rotor radial position using fixed point iteration with relaxation, as detailed in Section 4.3.

Chapter 5

Numerical modeling framework

This chapter explains the adaptation of the UMM in a MATLAB environment, specifically tailored for MOST (Matlab for OFWT Simulation Tools) framework [33], and outlines the methodology for comparative analysis used to verify the model. The emphasis is on how UMM is converted and adapted for MATLAB to enhance the aerodynamic simulation capabilities of MOST. Furthermore, this chapter explores the preliminary steps and methodologies for the comparative analysis, describing the selection process for the simulation site, the choice of turbine model, the acquisition of local meteorological conditions, and the computational strategies employed to estimate turbine productivity and the models' computational cost.

5.1 UMM adaptation in MATLAB

A portion of the thesis involved the contribution to adapting the UMM code, originally developed at MIT and accessible as an open-source Python library [34], into a MATLAB environment. The most challenging part of this process has been the instability of the mathematical model described in Section 4.3.1: iterative solvers often fail to converge when evaluating wake pressure, resulting in numerical divergence, especially at higher thrust coefficients. The code adaptation temporarily bypasses the numerical instabilities encountered with iterative solvers by incorporating the non-linear pressure data from the original Python implementation into a look-up table. This table is utilized during MATLAB simulations to interpolate pressure values directly, providing stable, pre-computed results for complex scenarios. Figure 5.1 presents a comparative visualization of the UMM against classical momentum theory across the five key equations of the model, specifically Equations 4.9, 4.15, 4.18, 4.21, and 4.36. These plots underscore the differences

in rotor-normal induction factor, streamwise wake velocity, lateral wake velocity, near-wake length, and wake pressure drop, highlighting UMM enhancements to aerodynamic simulations, especially concerning the wake. Specifically, discrepancies in trends regarding the induction factor and components of wake velocity are more pronounced at higher thrust coefficients. Furthermore, unlike classical momentum theory, the UMM successfully predicts near-wake length and wake pressure drop.

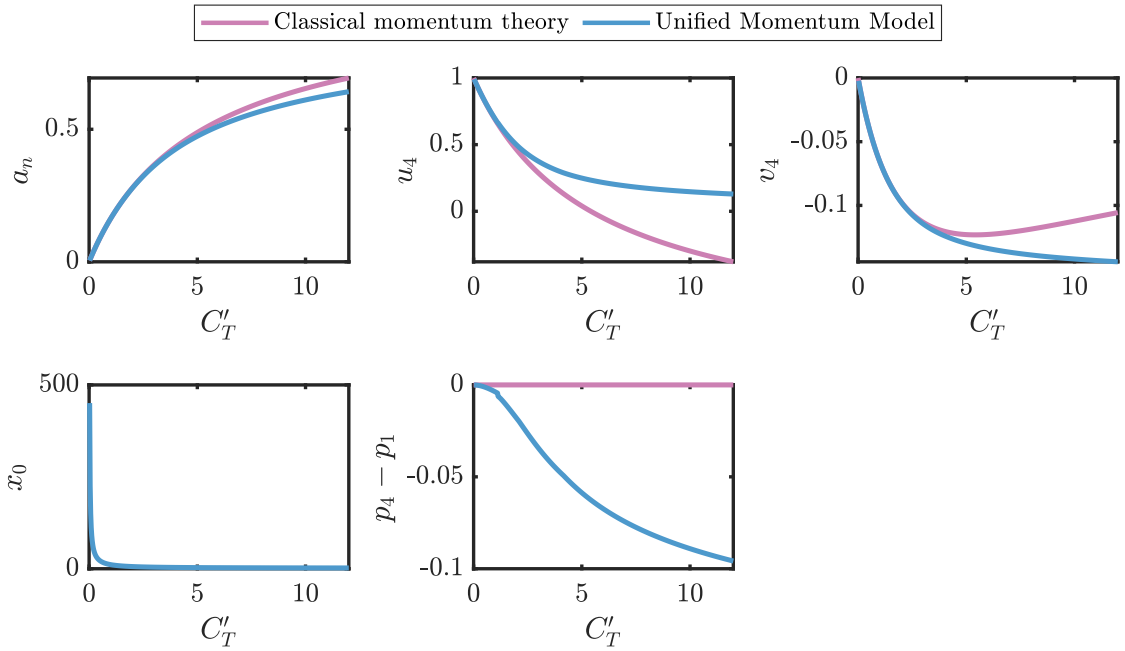

Figure 5.1: Classical momentum theory vs UMM behavior across the five equations of the model.

5.2 Integration of the UMM into MOST

The code migration was undertaken to integrate UMM into MOST, a simulation tool developed by MOREnergy Lab. MOST operates within the WEC-Sim environment, an open-source MATLAB/SIMULINK-based software for simulating wave energy converters. WEC-Sim utilizes the Simscape Multibody dynamics solver to model the behavior of these systems [35]. MOST is designed to simulate various configurations of offshore energy systems, including OFWTs, hybrid wind-wave energy converters, platforms equipped with multiple turbines and actively controlled water ballast[35].

Compared to existing simulation tools, such as OpenFAST (a state-of-the-art open-source software developed by the National Renewable Energy Laboratory (NREL) for offshore wind turbines [36]), MOST represents a more flexible and

easy-access tool. Furthermore, given the integration of such model with the WEC-Sim tool, it ensures an easy integration within the simulation framework of any hydrodynamic floating solution, even wave energy systems. Additionally, comparative studies, such as the one conducted by L. Cottura et al., demonstrate that MOST can replicate FAST's simulation results with remarkable accuracy (achieving a Root Mean Square Error (RMSE) of less than 2% for position and output power) [37]. To reduce computational time, MOST offers an alternative to simplify aerodynamics calculations: while FAST computes the pressure distribution along the blade at each node and performs iterative cycles to resolve aerodynamic forces, in MOST it is possible to decide whether to adopt the same approach or a different one. In the latter case, MOST generates, during the pre-processing phase, look-up tables for the aerodynamic loads (thrust and torque) as a function of blade pitch. This strategy reduces simulation times by a factor of three to five compared to FAST [33]. Such an approach is considered a good compromise between computational efficiency and accuracy, making it particularly suited for applications like design optimization, where preliminary designs must be explored efficiently. Unlike FAST, MOST is explicitly intended to follow this rationale, which enables faster and more flexible design iterations [38].

The primary motivation for adapting UMM to Matlab was to enhance the aerodynamic simulation capabilities within MOST. Traditionally, MOST relies on the classical BEM theory to model aerodynamics. While effective, BEM requires empirical corrections to address the shortcomings of classical momentum theory, especially under complex operational conditions. Furthermore, MOST does not currently account for wake deflection due to the rotor misalignment of the wind, and for wake dynamics [39].

By integrating the UMM, which does not rely on empirical adjustments, MOST gains a more accurate and reliable aerodynamic model. This enhancement is particularly crucial for FOWTs simulation since traditional theories often fail under the complex conditions where offshore turbines operate (high-thrust and yaw-misaligned states). UMM refines MOST's capability to predict rotor aerodynamics effectively across various challenging conditions, which is crucial for modeling the dynamic interactions of wind, waves, and floating structures.

In the adaptation of the UMM within the MOST framework, some modifications to the MOST library have been implemented. Particularly, a new child block named *UMM-integrated BEM* has been introduced to the *Aeroloads* Variant Subsystem block, illustrated in Figure 5.2. This subsystem is part of the *Aerodynamics + Control* subsystem within the *Wind Turbine* Simulink model, as shown in Figure 5.3.

Previously, the calculation of aerodynamic loads within MOST could be conducted either via look-up tables (LUT) or through a traditional BEM model. The

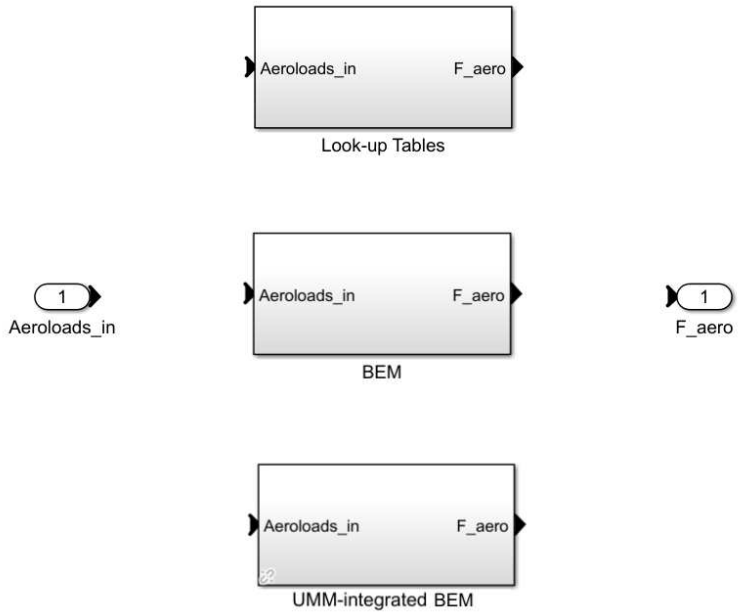

Figure 5.2: Aeroloads subsystem model.

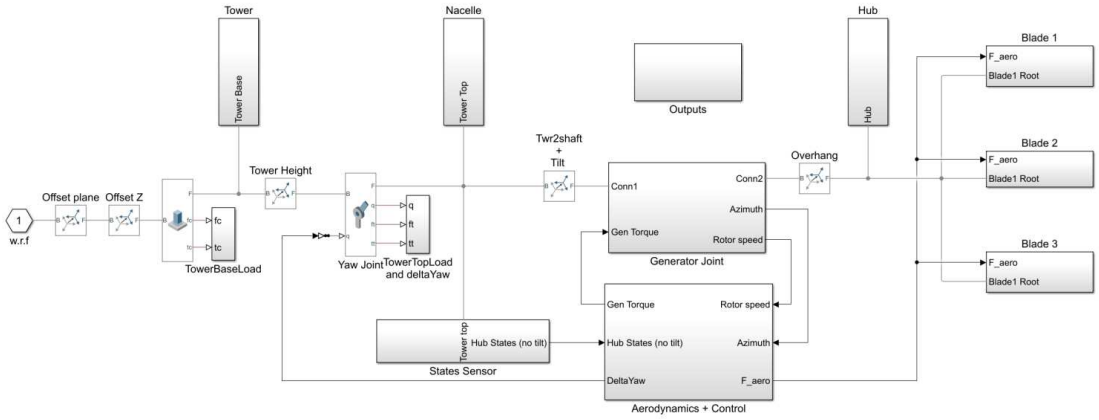

Figure 5.3: Wind Turbine Simulink library.

introduction of the *UMM-integrated BEM* variant offers an additional option, enabling the computation of aerodynamic forces through the UMM-enhanced BEM model at each simulation time step. Detailed documentation on the Simulink Wind Turbine model is available in the tool guide [35]. The *UMM-integrated BEM* block, whose internal structure is shown in Figure 5.4, mirrors the traditional BEM block, but incorporates a key difference in the MATLAB function. The function BEM_{UMM} within this block adapts BEM calculations to include UMM, primarily

affecting the momentum theory components. By integrating this new aerodynamic

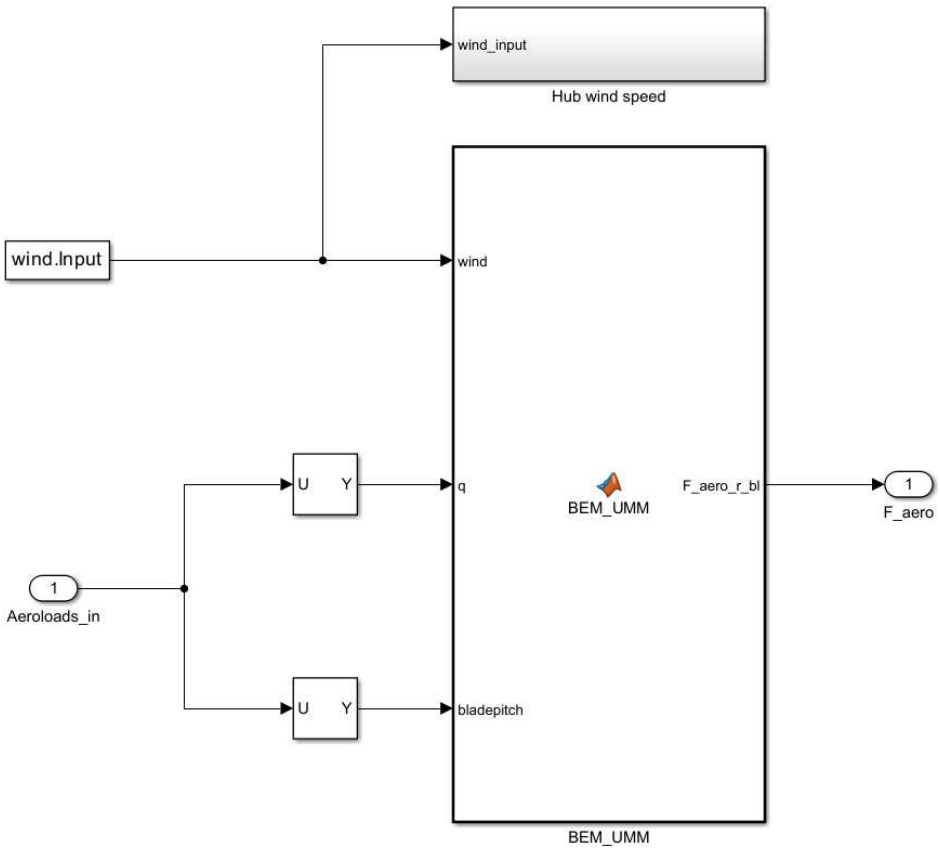

Figure 5.4: UMM-integrated BEM Simulink subsystem.

model in a modular and selectable Simulink system, users gain the flexibility to choose the most appropriate aerodynamic model for their simulations. This adaptability is crucial during the model verification process, which is performed through comparative analysis.

5.3 Comparative analysis

A case study approach is adopted to verify the aerodynamic model. The objective is to perform a comparison of the traditional MOST model, and its UMM-integrated version. The comparative analysis is carried out on turbine productivity and computational cost at a specific site.

5.3.1 Siting

The initial step for the comparison is site selection. Italy represents the world's third potential floating wind market, with an estimated floating potential of 207.3 GW, accounting for 97% of the Nation's wind energy potential [40]. The selected site is Pantelleria, an Italian island located in the Sicily Channel (110 km southwest of Sicily and 65 km northeast of Tunisia). Pantelleria is one of the windiest areas in Italy, as illustrated in Figure 5.5.

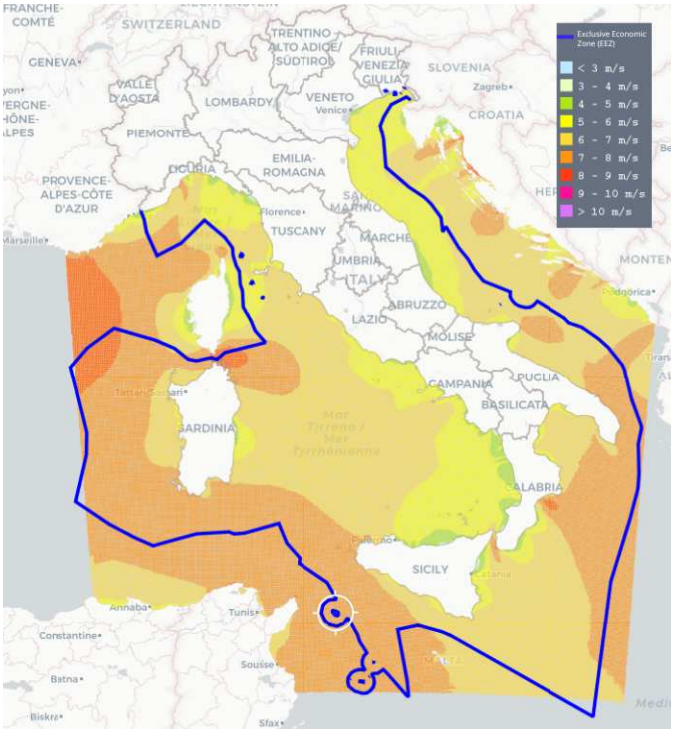

Figure 5.5: Annual mean wind speed at 100 m asl in Italy. Adapted from [41].

This location was selected for several reasons, each emphasizing its suitability for renewable energy projects. Firstly, Pantelleria is the largest among the "small islands" in Italy. Being a small island, it is not connected to the national electricity grid, thus it has to be self-sufficient for both production and distribution of electricity. Currently, the island meets its energy demand (37.6 GWh per year) through a thermoelectric power station, supplemented by a few small photovoltaic parks [42], but the electricity produced on the island is six times more expensive compared to the mainland price [43]. Since Pantelleria is characterized by a high availability of Renewable Energy Sources (RES), especially wind and solar, their implementation could contribute to solving this problem. Secondly, Pantelleria is one of the pilot sites for the WIMBY (Wind In My Backyard) project [44],

highlighting its relevance for innovative wind energy solutions. Furthermore, the site holds particular interest for MOREnergy Lab, as the research group is awaiting approval from Italian authorities for a test area dedicated to floating offshore wind simulations in the region [45].

The location coordinates for the case study are: 36 ° 59'15 " N, 11 ° 52'50 " E. To select the exact location, several aspects are considered:

- **Wind resource**: great exposure to the mistral, with a mean wind speed of 7-8 m/s at 100 meters of elevation, as shown in Figure 5.6.
- **Bathymetry**: the minimum water depth for floating wind turbines is 50 m. Each floating platform, however, has specific constraints. The platform with the tightest limit is the Spar type, due to the large draft, with a required minimum water depth of 150 m. As for the maximum water depth, the limit is 500 m for the same platform. Obviously, with increasing depths, mooring costs increase.
- **Distance from shore**, as a trade-off between the need to mitigate visual impact and to avoid excessive installation and OPEX costs: the minimum distance is 12 km for 5 MW turbines and 20 km for 15 MW turbines [2]. The maximum distance, according to the report of the European Commission [46], is set at 200 km: greater distances would not be economically viable.
- **Population density near the site**: due to tourism inflows, the island population varies significantly among the seasons, with all-year residents that are around seven thousand, and a population that nearly doubles during summer [42].
- **Maritime traffic**: the main ship routes have been considered and carefully avoided. Outside of this, a maximum maritime traffic density of 3 $(hours/(km^2y)$ is set as a limit [2].
- **Presence of natural parks and military zones**: all the marine protected zones and areas of military interest must be avoided.
- **Electric connection**: the nearest part of the island is the Arenella area, an industrial zone with low landscape and tourist value. Pantelleria's thermoelectric power station is located in this area, and future energy storage systems might be constructed here. Connecting an offshore wind farm here would allow easy electricity distribution into the grid or store it in case of production surplus [45].

Table 5.1 shows the site's characteristics.

Table 5.1: Characteristics of the site.

Site characteristics	
Mean wind speed (100 m asl)	7.69 m/s
Water depth	280 m
Distance from shore	18 km

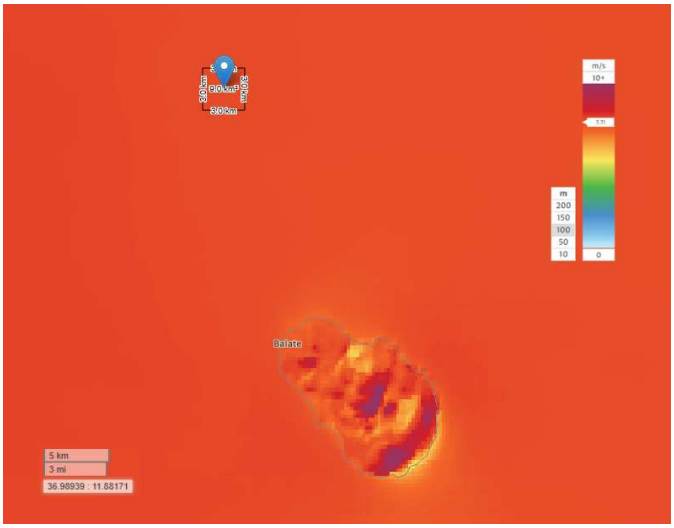

Figure 5.6: Annual mean wind speed at 100 m asl near Pantelleria. Adapted from [47].

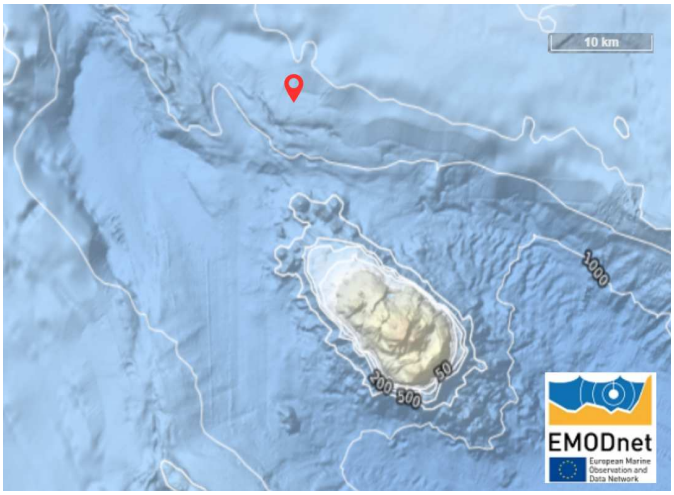

Figure 5.7: Bathymetry. Adapted from [48].

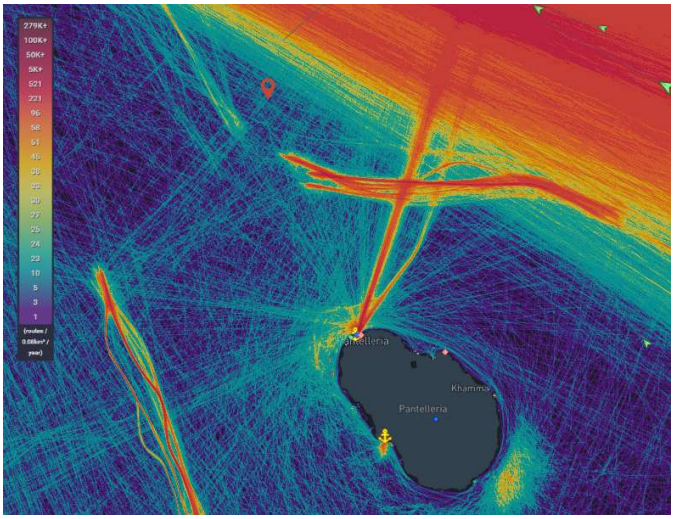

Figure 5.8: Marine traffic near Pantelleria. Adapted from [49].

5.3.2 Turbine selection

Considering the limited energy demand of the island, the NREL 5 MW reference wind turbine [50] was selected for the case study. The key parameters of the turbine, developed by the NREL, are shown in Table 5.2.

Table 5.2: NREL 5 MW reference turbine. Adapted from [50].

Turbine properties	
Rated power	5 MW
Rotor orientation and configuration	Upwind, 3 blades
Control	Variable speed, collective pitch
Drivetrain	High speed, multiple-stage gearbox
Rotor, Hub diameter	126 m, 3 m
Hub height	90 m
Cut-in, rated, cut-out wind speed	3 m/s, 11.4 m/s, 25 m/s
Cut-in, rated rotor speed	6.9 rpm, 12.1 rpm
Rated tip speed	80 m/s
Rotor mass	110 t
Nacelle mass	240 t
Tower and monopile mass	522.62 t

As justified in Chapter 2, the turbine is mounted on the Spar platform, shown in Figure 5.9. Moorings consist of a catenary system composed of three lines. A

Figure 5.9: Spar platform. Adapted from [37].

detailed explanation of different mooring systems for FOWTs can be found at [51].

5.3.3 Environmental conditions

To simulate wind and wave conditions, a dataset of the hourly data for the years 2021 and 2022 was extracted from the ERA5, a website of climate reanalysis produced by the European Centre for Medium-Range Weather Forecasts (ECMWF) [52]. The downloaded data are:

- u_{100}: 100 m u-component of wind;
- v_{100}: 100 m v-component of wind;
- H_s: significant height of combined wind waves and swell;
- T_p: peak wave period;
- dir_m: mean wave direction.

Appendix A contains a detailed explanation of sea state definition. Figure 5.10 and 5.11 show respectively the wind and the wave roses. As expected for its geographical location (situated between Sicily and Tunisia, hence shielded to the east by the former and to the west by the latter), Pantelleria is mainly exposed to two winds: the mistral, a northwesterly wind, and the sirocco, from south-east, reflecting the prevailing wind directions at site location. Waves' direction and strength mostly follow wind directions. Following the approach of Petracca et al. [39], a set of triplets was obtained from all possible combinations of wave height, wave period,

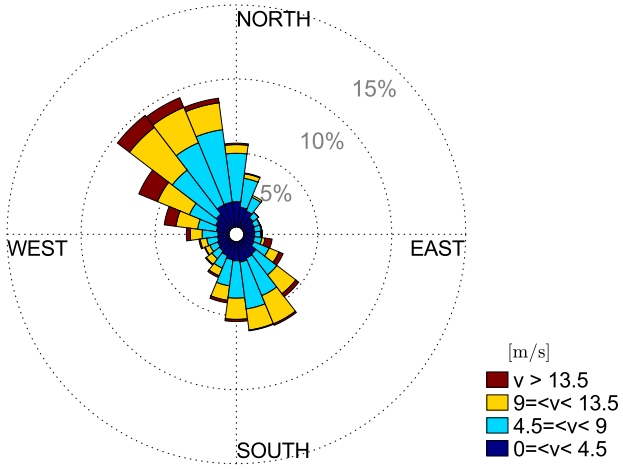

Figure 5.10: Wind rose at site location.

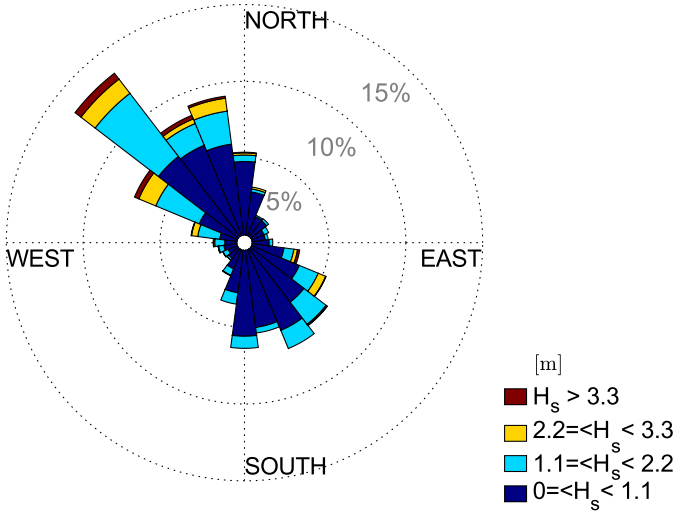

Figure 5.11: Wave rose at site location.

and wind speed, corresponding to 4,914 records. Starting from meteorological data gathered from ERA5, a wind scatter was obtained, following a similar approach to the one explained in section A.4 of Appendix A for wave scatters. Then, triplets were obtained by assigning the most probable sea state (in terms of significant wave height and peak wave period) to each wind speed. A scatter matrix of the triplets and the occurrences is shown in Figure A.7. The sea states at the case study location are characterized using the JONSWAP spectrum, which is tailored for enclosed seas like the Mediterranean. Further details on wave scatters and wave spectra are available in Appendix A. The number of triplets was then reduced by collecting triplets with the same wind speed, to avoid repetition with the same

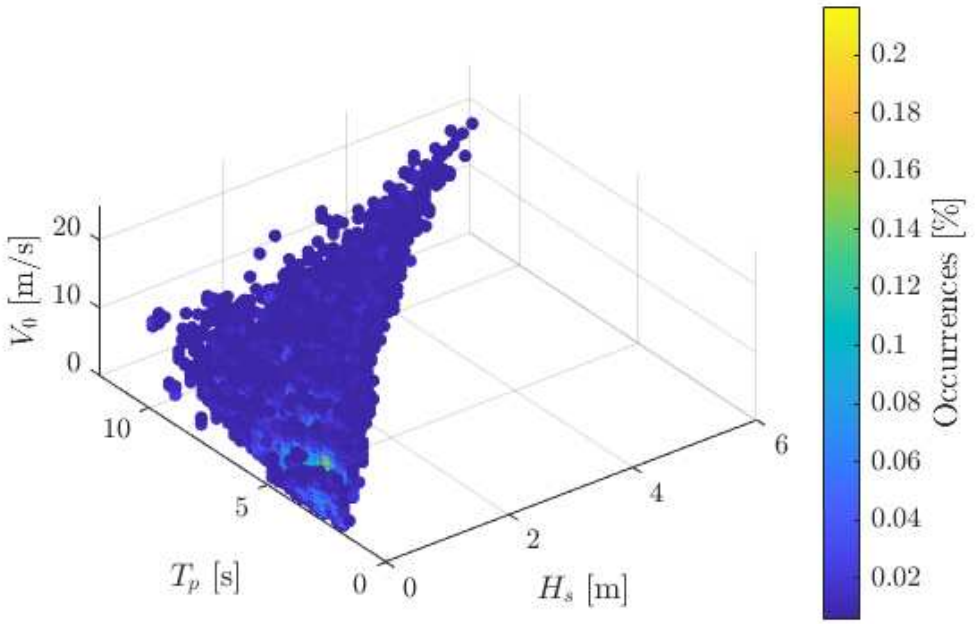

Figure 5.12: Scatter matrix of wind and wave data at site location.

wind speed and different wave conditions: a weighted average among the wave data associated with the given wind speed was assigned for each wind speed. Table 5.3 shows the reduced triplets used for the comparative analysis.

Figure 5.13 shows the occurrence of the wind speed in the site.

5.3.4 Methodology

After analyzing the transient behavior of the signal, it was decided to perform a 500-second time domain simulation for each triplet specified in Table 5.3 to evaluate turbine productivity. Given that the transient dissipates after 200 seconds, the subsequent 300 seconds are of stable readings. This approach balances accuracy with time efficiency. From each simulation, the mean power, denoted as P_i^{mean}, is calculated, representing the average power output at the wind speed associated with the i^{th} triplet. The Annual Energy Production (AEP) is then estimated using the following equation:

$$AEP = \sum_{i}^{N} P_i^{mean}(occ_i \cdot 60 \cdot 60 \cdot 24 \cdot 365)[J], \tag{5.1}$$

Table 5.3: List of triplets used for the simulations.

$V_0[m/s]$	$H_s[m]$	$T_p[s]$	$occ[-]$
0	0.3908	4.533	0.0116
1	0.3934	4.696	0.0382
2	0.4410	4.857	0.0531
3	0.4967	4.931	0.0634
4	0.5586	5.191	0.0693
5	0.6172	5.189	0.0728
6	0.6732	5.150	0.0752
7	0.7648	5.175	0.0691
8	0.8745	5.235	0.0705
9	1.014	5.494	0.0692
10	1.174	5.671	0.0687
11	1.337	5.867	0.0655
12	1.561	6.193	0.0573
13	1.873	6.691	0.0522
14	2.028	6.779	0.0392
15	2.408	7.463	0.0344
16	2.694	7.755	0.0274
17	2.910	7.906	0.0205
18	3.289	8.436	0.0193
19	3.727	8.935	0.0116
20	3.832	8.777	0.0073
21	4.208	9.181	0.0018
22	4.330	8.852	0.0022

where occ_i represents the annual fraction of time that each wind speed occurs. Subsequently, the Capacity Factor (CF) is calculated to determine the operational efficiency of the wind turbine relative to its rated power:

$$CF = \frac{AEP}{AEP_{rated}} = \frac{\sum_i^N P_i^{mean} occ_i}{P_{rated}}. \tag{5.2}$$

It should be noted that the CF values obtained in this study are likely to be overestimated. This overestimation arises because the simulations model only a single turbine, thus ignoring the wake effects typically observed in wind farms. Additionally, the model simplifies several aspects by omitting considerations such as cable losses, maintenance downtime, and turbulence. Wind turbine productivity is estimated for both aerodynamic theories for a fully aligned wind and for different inclinations of wind misalignment. Although the deep waters of the chosen site

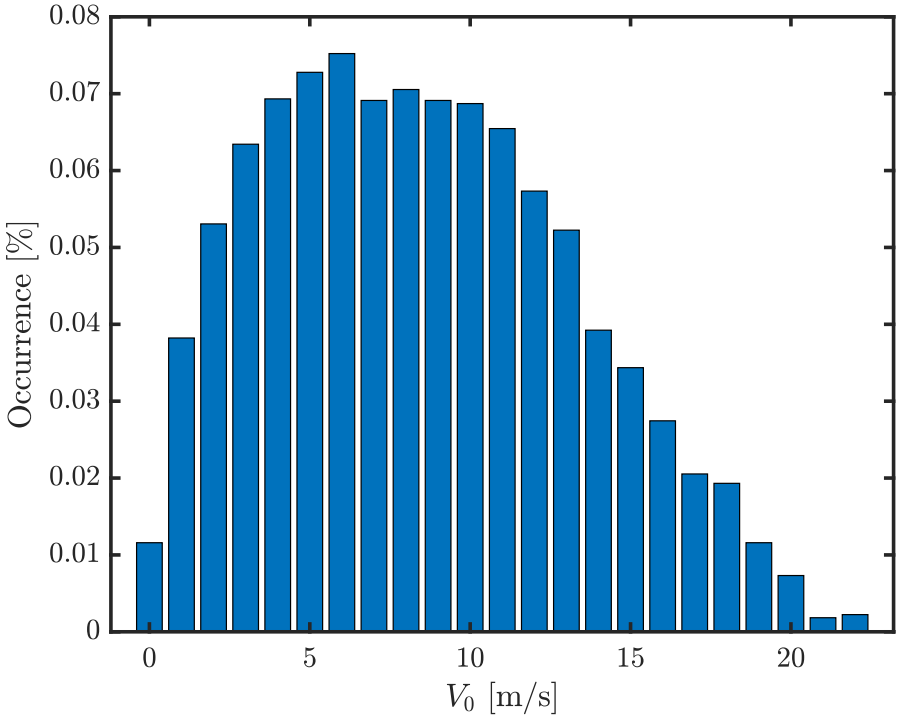

Figure 5.13: Wind speed occurrence at site location.

require a floating wind turbine, simulations have also been conducted for a fixed version of the same turbine. This step is deemed functional for a better understanding of the different behaviors of the two theories. The simulations assume a constant in-space wind field, implying that the wind characteristics are uniform across the domain. However, variability can be introduced by defining a timeline of instants at which the wind speed, azimuth, and elevation angles change, interpolating linearly between these points. To incorporate turbulence into the model, wind speed at each time step and across each node of the spatial grid covering the rotor area could be generated using TurbSim, a tool developed by the NREL, and integrated within the MOST framework [35, 53].

Chapter 6

Model verification

This chapter explores and discusses the outcomes of the analysis performed to verify the model. The analysis consists of three main parts, discussed in each section of this chapter. Section 6.1 shows a static comparison between different thrust-induction closures to BEM, performed to explore the discrepancies in power coefficient predictions and optimal control strategies among different momentum models. Section 6.2 delves into a comparative analysis of power curves, carried out by contrasting the enhanced MOST framework with its traditional version. Section 6.3 explains the outcomes of a time domain analysis on thrust and tower base loads, that is performed to further understand the different behavior of the two aerodynamic models. The objective of the comparative analysis is to assess the performance, computational efficiency, and fidelity of the UMM aerodynamic simulations under various operational conditions representative of real-world offshore floating wind turbine applications, and to critically analyze these findings by comparing them with traditional MOST simulations.

6.1 Static analysis

Before performing the comparative analysis in MOST, it was deemed appropriate to conduct a static analysis of the behavior of different BEM theories applied to the wind turbine chosen for the case study, the NREL 5MW [50]. This analysis was performed in Python, examining the aerodynamic behavior in terms of power coefficient C_P, for three different thrust-induction momentum modeling closures for BEM (classical momentum, classical momentum with high-thrust correction, and UMM), in three conditions: fully aligned wind and a wind misalignment of 30° and 45°, resulting in nine cases. Figure 6.1 thus displays contour plots of the variation of power coefficient C_P with blade pitch angle θ_p and blade TSR λ for the aforementioned cases. The maximum power coefficient $C_{P,max}$ in each simulation

is highlighted with a marker, and its coordinates are reported in the legend. All models incorporate the blade element model's Prandtl tip and root correction [16, 17].

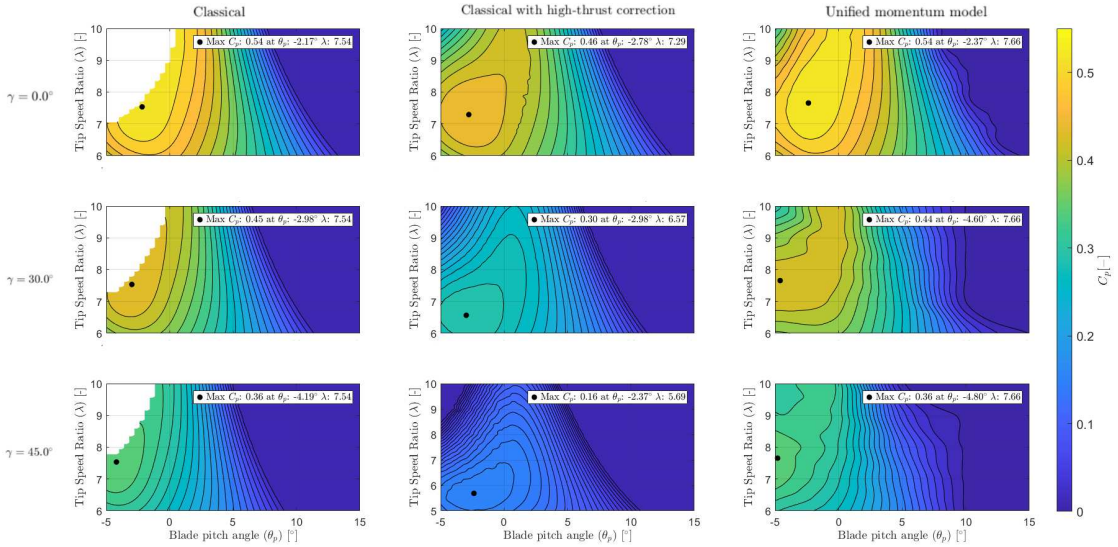

Figure 6.1: BEM modeling for the NREL 5MW turbine with different momentum theories.

Using a BEM model that relies on traditional one-dimensional momentum theory without modifications for high thrust (as shown in the first column of Figure 6.1) does not achieve convergence in areas where the thrust coefficient is above one. As a result, the highest achievable power coefficient $C_{P,max}$ is positioned at the boundary of model convergence, which complicates the determination of an optimal control point. The introduction of an empirical correction for high thrust addresses this issue by enabling the representation of the upper-left quadrant on the power coefficient surface, thus facilitating the determination of a globally optimal control setting. Nevertheless, this method introduces a degree of uncertainty due to its empirical basis. Switching from the classical momentum theory with its empirical adjustments to the UMM facilitates accurate predictions of the power coefficient over all necessary ranges of pitch and tip speed ratios, thereby allowing for the formulation of an optimal control strategy without employing empirical adjustments.

In scenarios of yaw misalignment, there is a noticeable reduction in the magnitude of the C_P contours in all cases, but the models differ in the identification of the optimal control strategy. As shown in Table 6.1, according to the traditional theory with high-thrust adjustment, the optimal control point reveals a reduced TSR under rotor misalignment, indicative of decreased thrust. In contrast, the UMM

Table 6.1: Maximum power coefficients for classical and UMM-integrated BEM models at 0°, 30°, and 45° yaw.

Aerodynamic model	γ	$C_{P_{max}}$	$\theta_{p_{C_{P,max}}}$	$\lambda_{C_{P,max}}$
Classical BEM with corrections	0°	0.46	−2.78°	7.29
	30°	0.30	−2.98°	6.57
	45°	0.16	−2.37°	5.69
UMM-integrated BEM	0°	0.54	−2.37°	7.66
	30°	0.44	−4.60°	7.66
	45°	0.36	−4.80°	7.66

shows a reduction in pitch angle with misaligned yaw, which correlates with an increase in thrust. This enhanced thrust is in agreement with existing literature that associates optimal wind turbine control under yaw misalignment with elevated thrust levels [6].

6.2 Power curve comparison

This section presents the results of the comparative analysis between the traditional version of MOST and the UMM-integrated version, focusing on turbine productivity and computational cost at the chosen site for the case study.

Figure 6.2 illustrates the sensitivity analysis derived from the comparison. Using

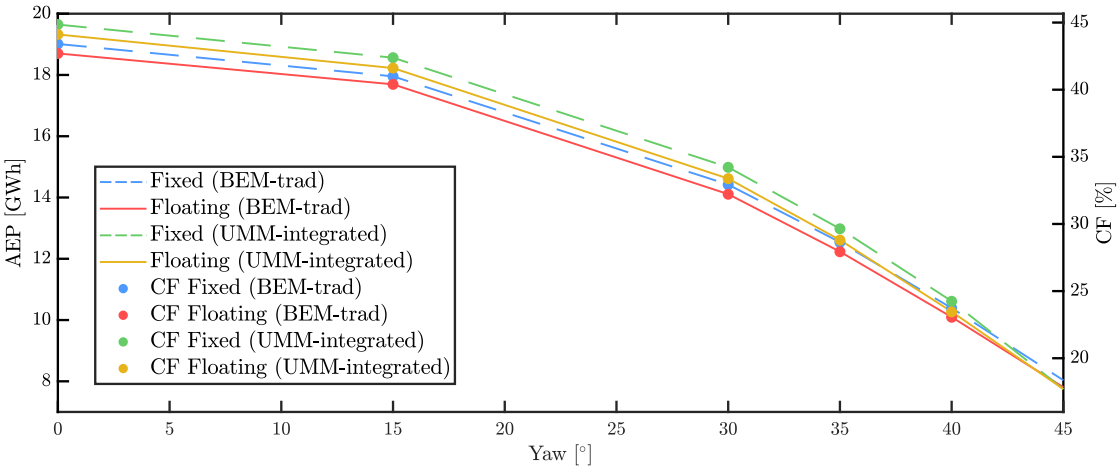

Figure 6.2: Sensitivity analysis on wind turbine productivity.

both aerodynamic theories, productivity for the fixed configuration proves slightly

superior to that of the floating configuration, regardless of wind direction. This outcome is anticipated, as floating turbines suffer more energy losses due to their dynamic response to ocean currents and waves. Moreover, simulations utilizing the UMM-integrated version of MOST demonstrate marginally higher productivity compared to those employing the traditional aerodynamic model. This improvement corresponds to the larger area of higher C_P values observed in the UMM case compared to the classical theory with empirical corrections, as depicted in Figure 6.1. An exception to this behavior occurs with simulations exhibiting yaw angles greater than 40°. In these cases, the UMM predicts slightly lower productivity values than the traditional model. This deviation warrants further investigation to understand the underlying dynamics affecting turbine performance at higher yaw angles. At this moment, it is reasonable to assume that this behavior is linked to the different control strategies that the two theories conduct to find the optimal operating point, which was evident from the results of the static analysis of Section 6.1. For fully aligned wind conditions, the CFs are predicted to be 42.70% for the traditional model and 44.12% for the UMM-integrated model. These values align with the expected performance for Pantelleria as outlined in Ghigo et al. [8]. Several simulations have been performed to evaluate computational time, considering fully aligned wind conditions and both fixed and floating configurations. Findings show that the UMM-integrated model requires twice the simulation time compared to MOST traditional version to evaluate turbine productivity. The higher computational cost is mostly related to two factors: the UMM performs additional iterations, which are then nested in traditional BEM iterative solution, while traditional momentum theory is much simpler; the UMM has a broader range of validity, while traditional BEM often utilises empirical corrections to bypass regions where classical momentum theory cannot be applied.

6.3 Time domain analysis

The final phase of the model verification involves a time domain analysis conducted in MOST, in its traditional version, and in the UMM-integrated one. This analysis evaluates the thrust force and loads at the weld joint of the tower base under two specific wind conditions: fully aligned and a 45° misalignment. The simulations consistently utilize the floating configuration of the same wind turbine, the NREL 5-MW reference model, across the previously characterized site. This setup ensures continuity of the operational conditions and variables introduced in earlier sections of the thesis. The metocean conditions selected for the time domain analysis are the rated wind speed, 11 m/s, with the corresponding sea state: a significant wave height of 1 meter, and a peak wave period of 6 seconds. Each simulation covers a span of 700 seconds, with the initial 100 seconds discarded to mitigate the influence

of transient behaviors.

Table 6.2 shows the mean power and the standard deviation of the signal for the four aforementioned cases. In this and all subsequent instances, the average quantities will be denoted by μ_{BEM} and μ_{UMM} for the values derived using the traditional version of MOST and the UMM-integrated version, respectively. Similarly, σ_{BEM} and σ_{UMM} will indicate the standard deviations of these quantities for each model. Comparing the simulation results obtained with the two aerodynamic models, the UMM-integrated version of MOST predicts a produced power that is, compared to the traditional MOST, $+7.54\%$ and -3.88% for the yaw-aligned and yaw-misaligned cases, respectively.

Table 6.2: Comparison of the power produced in rated-speed conditions.

γ	**Unit**	μ_{BEM}	μ_{UMM}	σ_{BEM}	σ_{UMM}
0°	MW	3.555	3.823	0.0149	0.0160
45°	MW	0.9899	0.9515	0.0094	0.0089

In the yaw-aligned scenario illustrated in Figure 6.3, the UMM-integrated BEM predicts a thrust force that is 4.5% higher than that predicted by the traditional model. Additionally, the two models produce thrust curves with different excitation frequencies, indicating that the turbines operate at distinct rotational speeds despite identical meteorological conditions. Figure 6.4 shows the same comparison but obtained for a misaligned wind of 45°. Contrary to the yaw-aligned case, the UMM-integrated model predicts a 6.9% reduction in thrust compared to the traditional BEM, exhibiting a lagging trend in the signal dynamics. Table 6.3 summarizes the mean thrust values and their standard deviations for both models under these wind conditions.

Table 6.3: Comparison of the thrust force in rated-speed conditions.

γ	**Unit**	μ_{BEM}	μ_{UMM}	σ_{BEM}	σ_{UMM}
0°	kN	161.6	168.9	7.179	7.226
45°	kN	72.78	67.80	21.19	19.22

Concerning the tower base loads, whose trends are shown in Figure 6.5 and whose meaningful values are depicted in Table 6.4, the main differences between the two models in the case of yaw-aligned wind manifest in the moments along the z-axis and x-axis, and in the force in the y-direction. Notably, the force along the z-axis remains unchanged between models, indicating that this load component

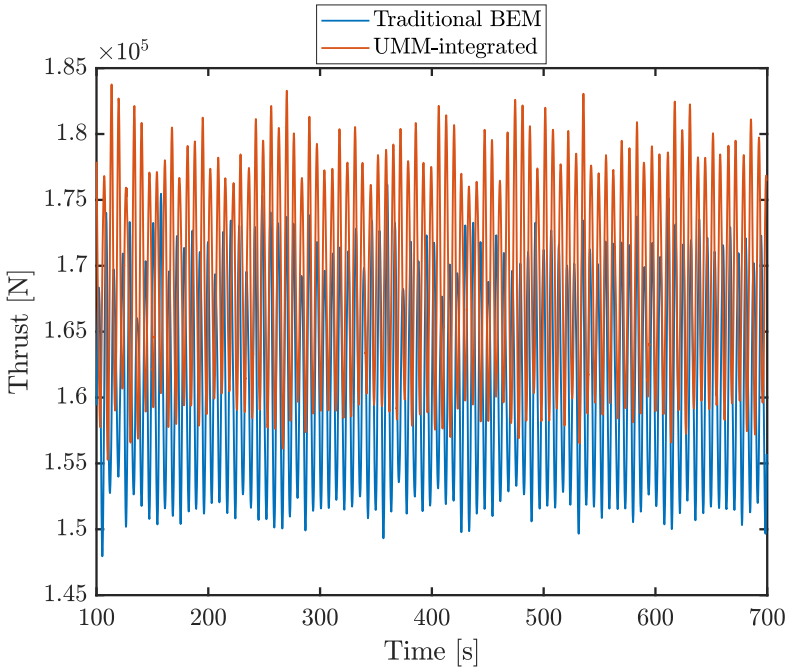

Figure 6.3: Thrust force for $\gamma = 0°$.

is unaffected by the choice of aerodynamic model. Moreover, the force in the y-direction is significantly smaller than that in the x-direction, consistent with the wind orientation primarily in the x-axis. Overall, the UMM-integrated version of MOST predicts higher loads for all six degrees of freedom, perhaps implying that traditional aerodynamic theory could underestimate loads. This underestimation could potentially lead to design or operational failures in real-world wind farm applications.

Performing the same analysis for a misalignment of 45° the force in the z-direction remains unaffected by the momentum theory utilised to perform the simulation, consistent with the findings from the aligned case. However, notable differences emerge in the force in the y-direction, and in the moments along the x- and y-axes. Moreover, the most significant discrepancies between the simulations consist in the much higher standard deviations found for the UMM-integrated model, particularly for F_x and M_z. This increased volatility suggests that the UMM model may be more sensitive to certain factors or that it incorporates dynamics not accounted for by the traditional model. Further analysis is necessary to determine the specific causes and implications of these discrepancies. In general, the differences in the outcomes of the time domain analysis stem from the different aerodynamic impact of the two momentum theories, in terms of both the control strategy and the dynamic effects that each aerodynamic model has on the system.

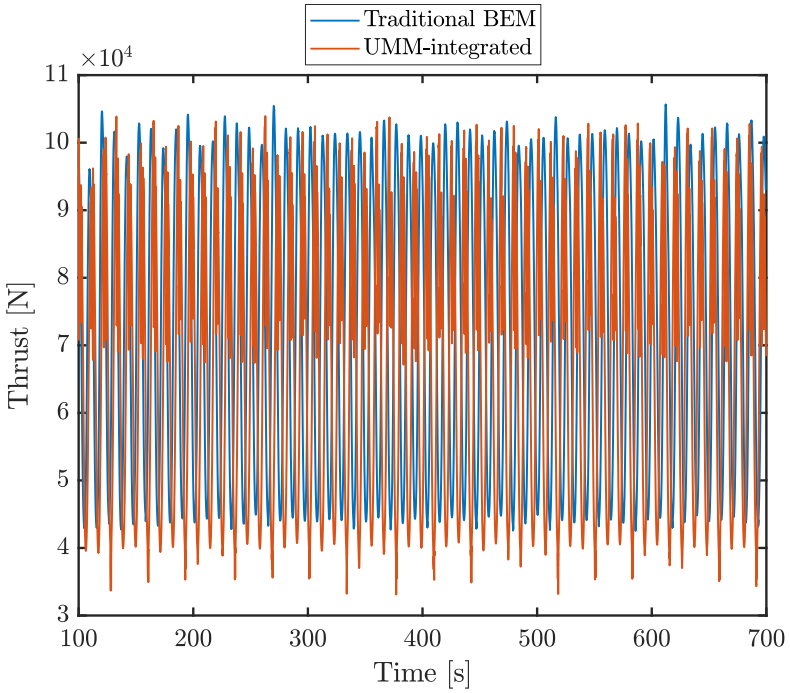

Figure 6.4: Thrust force for $\gamma = 45°$.

Table 6.4: Comparison of the tower base loads in rated-speed conditions.

γ	Load	Unit	μ_{BEM}	μ_{UMM}	σ_{BEM}	σ_{UMM}
0°	F_x	kN	923	965	57.7	57.6
	F_y	kN	-50	-52	14.8	15.8
	F_z	kN	-5908	-5908	4.4	4.5
	M_x	kNm	7433	7802	1004.5	1067.1
	M_y	kNm	70801	74120	4081.8	4078
	M_z	kNm	204	188	79.4	82.1
45°	F_x	kN	385	358	60.6	610
	F_y	kN	-8	-12	37.7	46.9
	F_z	kN	-5902	-5900	4.8	5.7
	M_x	kNm	2173	2440	2573.5	3206.7
	M_y	kNm	27221	25212	4309.8	4329.9
	M_z	kNm	165	163	66.8	113.1

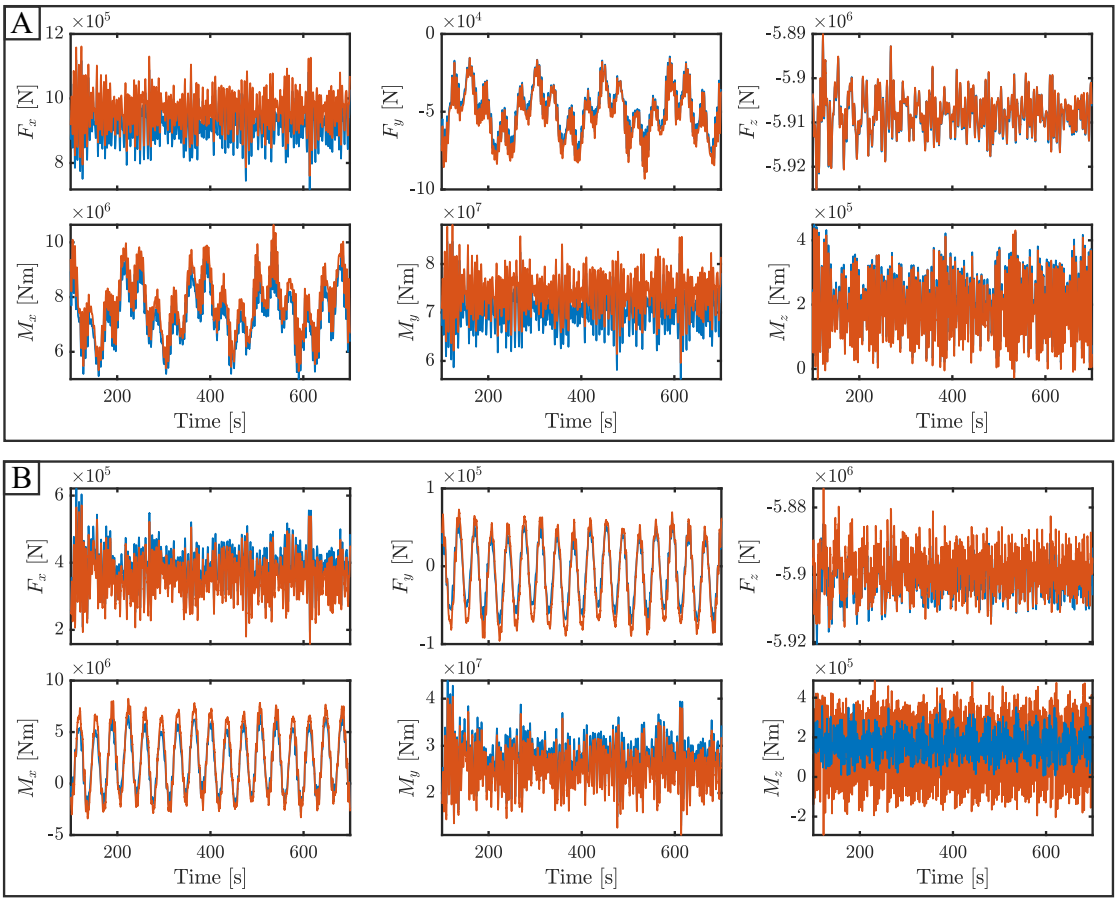

Figure 6.5: Tower base loads: $\gamma = 0°$ (A), $\gamma = 45°$ (B).

Chapter 7

Conclusion and future developments

The escalating global need for clean and sustainable energy has driven the growth and evolution of wind turbines, which are increasingly deployed offshore to harness more powerful and consistent winds. As these turbines grow in size and complexity, the inadequacies of classical aerodynamic models become more apparent, particularly under challenging conditions such as high thrust and yaw misalignment, where classical momentum theory requires empirical corrections to operate.

A recent breakthrough, the development of the UMM, eliminates the need for any empirical adjustment in favor of a more accurate and robust framework. This advancement enhances the predictive capabilities of aerodynamic simulations for offshore turbines, allowing for a new and improved BEM model able to work across all operating conditions of modern wind turbines.

This thesis has successfully integrated the UMM into MOST, enhancing its aerodynamic simulation capabilities. In contrast with other aerodynamic solvers, MOST represents a user-friendly tool capable of coupling aerodynamic and hydrodynamic problems in a MATLAB framework. This integration allows to fill the gaps in the current modeling techniques for offshore applications. Such aerodynamic improvement is particularly beneficial since MOST models offshore systems, that are known to work exactly in the regions where traditional aerodynamic models fail to operate.

The most significant findings from the comparison among the UMM-integrated version of MOST and the traditional one that relies on classic BEM are that the different aerodynamic models have a significant impact on AEP, with a maximum difference of 4% in productivity predictions obtained when the yaw is 30°, and on turbine base loads.

However, the study also uncovers areas requiring further investigation:

- the overlap of productivity results for fixed and floating configurations when the wind has 45° of misalignment. An investigation could consist of generating a static map for both cases, as the ones built in Section 6.1 of Chapter 6.
- the high standard deviation of the loads evaluated with the UMM-integrated version of MOST for winds with 45° of yaw.

Further developments could include:

- wake analysis, that would allow to fully understand the potentialities and implications of the new momentum theory since classical momentum theories completely ignored the wake pressure drop that is now modeled.
- a model validation, since this thesis only performed a verification through a comparative analysis approach, while it could be interesting to have some real data to cross-reference the simulation results and ensure reliability across a range of operating conditions.
- incorporating turbulence in the wind signal through the TurbSim tool, already integrated within the MOST framework.

Possible future applications could consist of applying the model for optimization purposes, exploiting the more detailed aerodynamic tool to obtain better designs, and using the wake simulation capabilities of the model to analyse wake losses and performances for wind farms.

In conclusion, the integration of this higher fidelity momentum theory into MOST marks a step forward in the simulation of offshore systems, with the potential to substantially impact future turbine design and deployment strategies.

Appendix A

Linear theory of ocean waves

Waves are created by a combination of various disturbing forces (such as wind, earthquakes, and gravitational pulls from the Moon and Sun) and restoring forces (such as surface tension and gravity). This analysis specifically addresses waves generated by wind interactions with the water surface. Initially, wind generates small capillary waves on the water surface, that are counteracted by the weak tension surface force. As capillary waves form, they provide a rougher surface for wind to blow on, so waves grow in height forming ripples. As the process continues, waves grow, transitioning into chop waves, characterized by their relatively short crest lengths. Eventually, the sea reaches full development, a state where wave height increases at a faster rate than wavelength, until reaching the critical steepness (the ratio between wave height H (which is the vertical distance of the wave crest from the wave trough) and wavelength $\bar{\lambda}$) of $1:7$. At this point the wave breaks, generating the phenomenon of white capping. The progression from initial formation to fully developed sea depends on both the wind speed and the fetch, that is the distance over which the wind has been blowing. Figure A.1 illustrates wave classification according to the wave period (which identifies the time taken by two successive wave crests for passing a fixed point), a classification proposed by Walter Munk [54]. Waves are generated from both local and distant weather systems (the latter case is true for swell waves). Therefore, they are the result of the superimposition of these two factors.

Several theoretical frameworks for understanding wave dynamics have been developed over time. Le Méhauté diagram, depicted in Figure A.2, explains the applicability range of different wave theories. For the scope of this analysis, only linear waves are considered, where Airy theory is applicable. This corresponds to the bottom-right portion of the diagram, characterized by a high relative water depth h/gT^2, and small wave steepness $\bar{s} = H/gT^2$. h is the water depth, g the

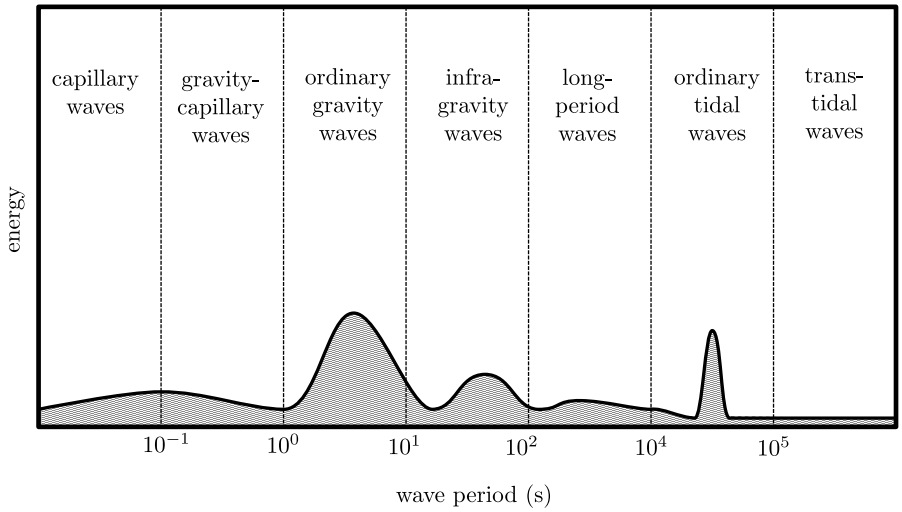

Figure A.1: Wave classification according to the wave period [54].

gravitational acceleration, and $\bar{T}$ the wave period. [1]

A.1 Regular waves

Regular waves are sinusoidal harmonic waves, which despite not existing in nature, serve as a fundamental basis for analyzing real sea state conditions. A regular wave, schematized in Figure A.3 can be defined by means of a wave period $\bar{T}$, and a wave height H:

$$\eta(t) = \bar{a}\sin(\bar{\omega}t + \bar{\varphi}), \tag{A.1}$$

where $\bar{a}$ represents the wave amplitude (defined as the distance from the still water level to the crest, which is half of the wave height), $\bar{\omega} = \frac{2\pi}{\bar{T}}$ is the wave frequency, $\bar{\varphi} \in [0,2\pi]$ is the wave phase, and $\eta(t)$ is the wave elevation.

Waves (and their associated wave period) are also classified according to the water depth, as shown in Figure A.4, to characterise the phenomenon according to which as a monochromatic wave propagates, it dissipates its kinetic energy due to friction of water particles with the sea bed. According to [56], the following relationships can be considered:

- deep water: $h > \bar{\lambda}/4$,
- shallow water: $h < \bar{\lambda}/25$,

[1] In this Appendix the overline notation is employed to distinguish between wave-related and wind-related parameters, ensuring clarity in both topics.

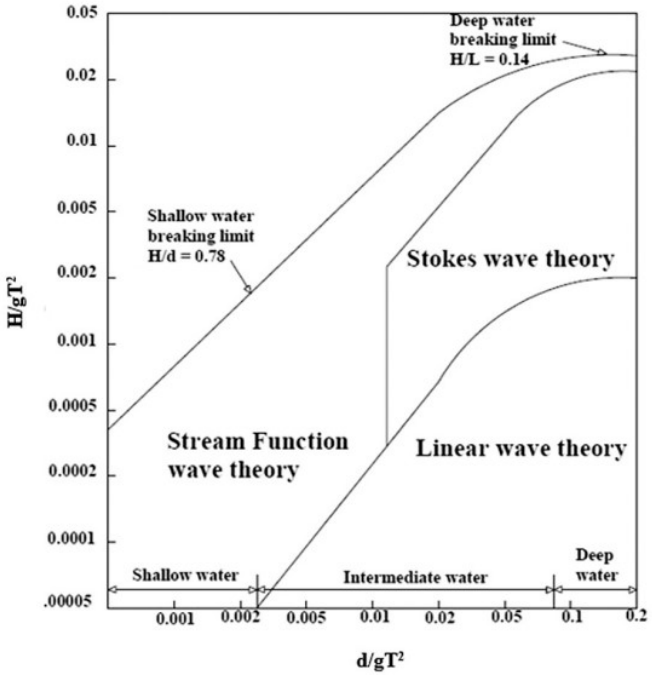

Figure A.2: Le Méhauté diagram. Reproduced from [55].

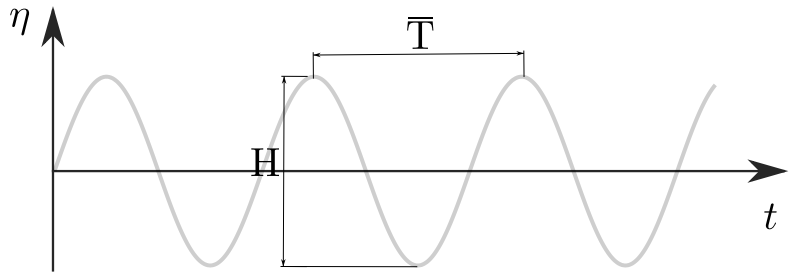

Figure A.3: Representation of a regular wave.

- transitional depth: $\bar{\lambda}/25 < h < \bar{\lambda}/4$.

Throughout this thesis, the deep water assumption was considered valid.

A.2 Irregular waves

In reality, ocean waves are irregular. They can however be represented as the superposition of sinusoidal (regular) waves with varying amplitudes, frequencies, and directions. This concept is mathematically represented in Equation A.2, where $\bar{a_i}$, $\bar{\omega_i}$, and $\bar{\varphi_i}$ are respectively the amplitude, the frequency, and the phase of the

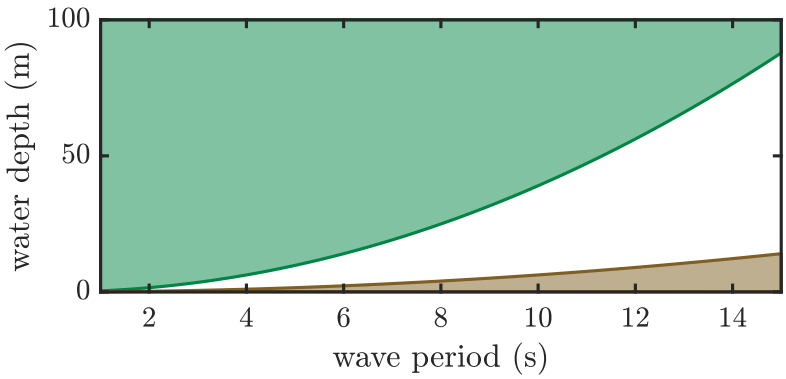

Figure A.4: Wave classification according to wave depth. In green, white, and brown are shown the deep water condition, the transitional depth condition, and the shallow water condition, respectively.

i-th wave.

$$\eta(t) = \sum_i a_i \sin(\omega_i t + \varphi_i). \tag{A.2}$$

Furthermore, it is known that the statistical distribution of a wave height record $\eta(t)$ is Gaussian [57]. This statistical analysis of a wave record allows the evaluation of significant parameters of a sea state, as:

- The significant wave height $H_{1/3}$, defined as the average height of the highest one-third of the waves of a wave record;
- The significant wave period $T_{1/3}$, generally associated to the peak of a wave spectrum;
- The maximum height of a record H_{max}, often considered equal to double the significant wave height.

These and other parameters are derived from a wave spectra description of the wave phenomena.

A.3 Spectral representation of ocean waves

Given the representability of real waves as the superposition of regular ones, and considering a discrete number of sinusoidal waves, with the linear theory, the wave energy density is the sum of the energy density of each sinusoidal wave, as:

$$E = \frac{1}{2}\rho g \sum_{i=1}^{N} \bar{a_i}^2. \tag{A.3}$$

Hence, Equation A.2 can be linked to the Fourier transform of a time series. Details about Fourier analysis can be found at [58]. Since the energy associated to a monochromatic wave is proportional to the squared wave amplitude it is possible to define a wave spectrum, represented in Figure A.5, that is the energetic representation of an irregular sea state.

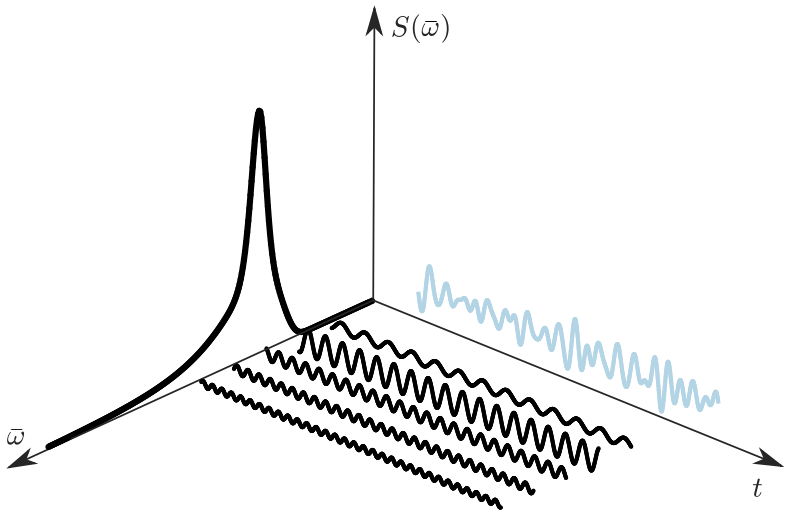

Figure A.5: Wave spectrum as superposition of monochromatic signals.

Among the different wave spectra elaborated to statistically represent a wave record, the most important are:

- The Bretschneider spectrum [59], commonly used to describe growing sea conditions;
- The Pierson-Moskovitz spectrum [60], a particular case of the previous one, limited to fully developed seas;
- The JONSWAP spectrum [61], adopted for enclosed seas, where waves have a limited fetch;
- Multimodal wave spectra, as Torsethaugen and Ochi-Hubble, employed for sites where the local wind effect is coupled with swell generated far away.

Being the geographical context of the thesis the Mediterranean Sea, a closed sea, waves are represented using the JONSWAP spectrum, that is a Pierson-Moskowitz spectrum multiplied by a peak enhancement factor, $\bar{\gamma}$, which defines the spectrum shape. Figure A.6 shows a graphical representation of the influence of the peak enhancement factor on the spectrum shape. The formulation of the JONSWAP spectrum is defined in Equation A.4, where $S(\bar{\omega})$ is the wave spectral density

function, c_1 is an empirical constant, $\bar{\gamma} \in [1, 7]$ is the peak-enhancement factor, and $\alpha(\bar{\omega})$ is the $\bar{\gamma}$ exponent:

$$S(\bar{\omega}) = \frac{c_1 g^2}{\bar{\omega}^5} e^{-1.25\frac{\bar{\omega}^4}{\bar{\omega}_p^4}} \bar{\gamma}^{\alpha(\bar{\omega})}. \tag{A.4}$$

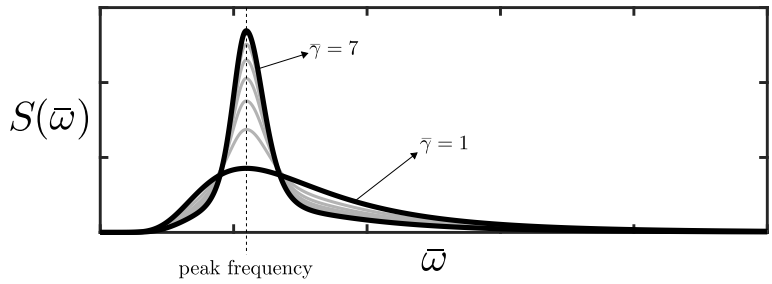

Figure A.6: Influence of the peak enhancement factor on the JONSWAP spectrum shape.

Among the characteristic parameters that can link the mathematical model to the statistical representation of a wave record, the n-th order spectral moment m_n is defined as:

$$m_n = \int_0^\infty \bar{\omega}^n S(\bar{\omega}) d\bar{\omega}. \tag{A.5}$$

This means that m_0 is the area under the spectral curve, m_1 is the static moment, and m_2 is the moment of inertia. Accordingly, it is possible to define the following characteristic properties of an associated wave spectrum:

$$T_e = \frac{m_{-1}}{m_0}, \qquad H_{m_0} = 4\sqrt{m_0}, \qquad J = \frac{\rho g^2}{64\pi} H_{m_0}^2 T_e. \tag{A.6}$$

T_e is the energy period, H_{m_0} is the significant wave height (being it equal to H_s and $H_{1/3}$), and J is the wave power density.

A.4 Wave scatters

Wave scatters are used to describe long-term metocean conditions at a particular site. They express the site properties, such as the occurrence of particular sea-states, as shown in Figure A.7. First, a large set of wave synthetic data, such as the peak wave period, the significant wave height, and direction are gathered. Then, this dataset is divided into bins to define the occurrence scatter O_ω. The scatter is often normalised over the total number of observations, hence the summation of all the occurrences is equal to 1. Once the occurrence scatter table is obtained, the

energetic scatter $O_{en_{i,j}}$ can be obtained by multiplying the occurrence scatter by the corresponding wave power density J, as in Eq. A.7:

$$O_{en_{i,j}} = JO_{\omega_{i,j}}. \tag{A.7}$$

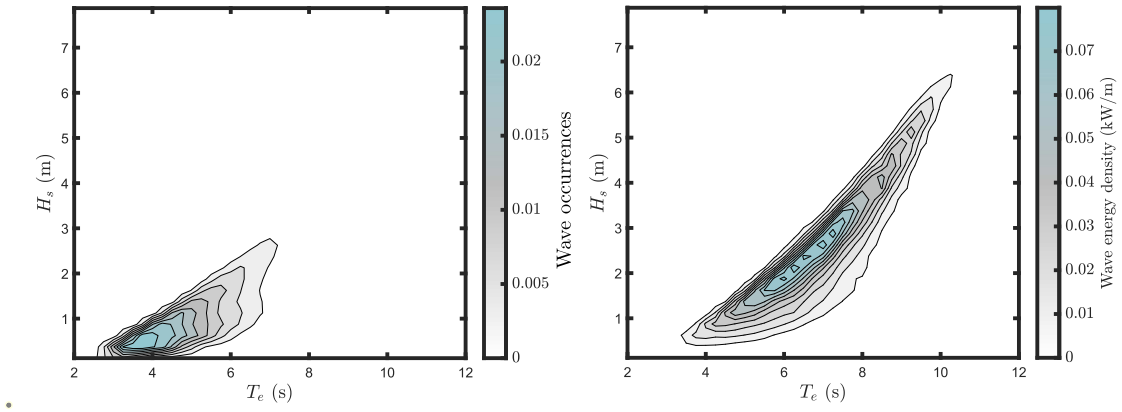

Figure A.7: Wave scatter for the Pantelleria site, Italy. Occurrences scatter (left), and energetic scatter (right).

Bibliography

[1] R. Williams and F. Zhao. *Global offshore wind report 2024*. Tech. rep. Global Wind Energy Council (GWEC), 2024 (cit. on p. 1).

[2] E. Faraggiana, A. Ghigo, M. Sirigu, E. Petracca, G. Giorgi, G. Mattiazzo, and G. Bracco. «Floating offshore wind potential for Mediterranean countries». In: *Heliyon* (2024). DOI: https://doi.org/10.1016/j.heliyon.2024.e33948. URL: https://www.sciencedirect.com/science/article/pii/S2405844024099791 (cit. on pp. 1, 6, 43).

[3] TEHA (The European House - Ambrosetti). *Floating Offshore Wind Community*. URL: https://www.ambrosetti.eu/en/our-communities/floating-offshore-wind-community/ (cit. on p. 1).

[4] H. A. Madsen, T. J. Larsen, G. R. Pirrung, A. Li, and F. Zahle. «Implementation of the blade element momentum model on a polar grid and its aeroelastic load impact». In: *Wind Energy Science* 5 (2020). DOI: 10.5194/wes-5-1-2020 (cit. on p. 1).

[5] A. Rajan and F. L. Ponta. «A Novel Correlation Model for Horizontal Axis Wind Turbines Operating at High-Interference Flow Regimes». In: *Energies* 12 (2019). DOI: 10.3390/en12061148 (cit. on p. 1).

[6] J. Liew, K. S. Heck, and M. F. Howland. «Unified momentum model for rotor aerodynamics across operating regimes». In: *Nature Communications* 15 (2024). DOI: https://doi.org/10.1038/s41467-024-50756-5 (cit. on pp. 1, 2, 11, 19, 20, 22, 23, 28, 33–35, 53).

[7] T. M. Letcher. *Wind Energy Engineering*. Academic Press, 2017 (cit. on pp. 2, 10).

[8] A. Ghigo, L. Cottura, R. Caradonna, G. Bracco, and G. Mattiazzo. «Platform optimization and cost analysis in a floating offshore wind farm». In: *Journal of Marine Science and Engineering* 8 (2020). DOI: 10.3390/jmse8110835. URL: https://www.mdpi.com/2077-1312/8/11/835 (cit. on pp. 3, 54).

[9] A. Bertozzi, F. Niosi, B. Paduano, and X. Jiang. «Perspectives on design of floating platforms for offshore airborne wind energy systems». In: Oct. 2024, pp. 627–634. ISBN: 9781003558859. DOI: 10.1201/9781003558859-69 (cit. on pp. 3, 5).

[10] M. Hannon, E. Topham, J. Dixon, D. Mcmillan, and M. Collu. *Offshore wind, ready to float? Global and UK trends in the floating offshore wind market*. Oct. 2019. DOI: 10.17868/69501 (cit. on p. 4).

[11] X. Mei and M. Xiong. «Effects of Second-Order Hydrodynamics on the Dynamic Responses and Fatigue Damage of a 15 MW Floating Offshore Wind Turbine». In: *Journal of Marine Science and Engineering* 9 (Nov. 2021), p. 1232. DOI: 10.3390/jmse9111232 (cit. on p. 5).

[12] R. James and M. C. Ros. «Floating offshore wind: market and technology review». In: *The Carbon Trust* 439 (2015) (cit. on p. 6).

[13] J.W. Rankine. «On the mechanical principals of the action of propellers». In: *Transaction of the Institute of Naval Architects* 6 (1865) (cit. on p. 7).

[14] W. Froude. «On the elementary relation between pitch, slip and propulsive efficiency». In: *Transaction of the Institute of Naval Architects* 19 (1878) (cit. on p. 7).

[15] E. R. Froude. «On the part played in propulsion by differences of fluid pressure». In: *Transaction of the Institute of Naval Architects* 30 (1889) (cit. on p. 7).

[16] J. Manwell, J. Mcgowan, and A. Rogers. «Wind Energy Explained: Theory, Design and Application, Second Edition». In: vol. 30. 2006. DOI: 10.1260/030952406778055054 (cit. on pp. 7, 11, 12, 17, 20, 52).

[17] P. J. Moriarty and A. C. Hansen. *AeroDyn Theory Manual*. 2005 (cit. on pp. 15, 20, 21, 52).

[18] P. Pratumnopharat and P. S. Leung. «Validation of various windmill brake state models used by blade element momentum calculation». In: *Renewable Energy* 36 (2011). DOI: https://doi.org/10.1016/j.renene.2011.03.027 (cit. on pp. 18, 21).

[19] A. Cooperman and M. Martinez. «Load monitoring for active control of wind turbines». In: *Renewable and Sustainable Energy Reviews* Vol. 41 (2014). DOI: 10.1016/j.rser.2014.08.029 (cit. on p. 19).

[20] L. Martinez-Tossas, E. Branlard, K. Shaler, and al. «Numerical investigation of wind turbine wakes under high thrust coefficient». In: *Wind Energy* 25 (2022). DOI: https://doi.org/10.1002/we.2688 (cit. on p. 19).

[21] P. A. Fleming, A. K. Scholbrock, A. Jehu, and al. «Field-test results using a nacelle-mounted lidar for improving wind turbine power capture by reducing yaw misalignment». In: *Conference Series* (2022). DOI: https://doi.org/10.1088/1742-6596/524/1/012002 (cit. on p. 19).

[22] P. Fleming, J. King, K. Dykes, E. Simley, and al. «Initial results from a field campaign of wake steering applied at a commercial wind farm – Part 1». In: *Wind Energy* (2019). DOI: https://doi.org/10.5194/wes-4-273-2019 (cit. on pp. 19, 21).

[23] H. M. Johlas, L. A. Martinez-Tossas, M. J. Churchfield, and al. «Floating platform effects on power generation in spar and semisubmersible wind turbines». In: *Wind Energy* (2021). DOI: https://doi.org/10.1002/we.2608 (cit. on p. 19).

[24] B. L. Marshall. *A New Empirical Relationship between Thrust Coefficient and Induction Factor for the Turbulent Windmill State*. Tech. rep. NREL, 2005 (cit. on p. 21).

[25] O. Gebraad, F. W. Teeuwisse, J. W. van Wingerden, and al. «Wind plant power optimization through yaw control using a parametric model for wake effects—A CFD simulation study». In: *Wind Energy* 19 (2015). DOI: https://doi.org/10.1002/we.1822 (cit. on p. 21).

[26] K.S. Heck, H.M. Johlas, and M.F. Howland. «Modelling the induction, thrust and power of a yaw-misaligned actuator disk». In: *Journal of Fluid Mechanics* 959 (2023). DOI: 10.1017/jfm.2023.129 (cit. on p. 24).

[27] L.M. Milne-Thomson. «Theoretical Aerodynamics». In: *Courier Corporation* (1973) (cit. on pp. 26, 27).

[28] M. Bastankhah and F. Porté-Agel. «Experimental and theoretical study of wind turbine wakes in yawed conditions». In: *Journal of Fluid Mechanics* 806 (2016). DOI: 10.1017/jfm.2016.595 (cit. on p. 27).

[29] H. A. Madsen. «An analytical linear two-dimensional actuator disc model and comparisons with computational fluid dynamics (CFD) simulations». In: *Wind Energy Science* 8 (2023). DOI: 10.5194/wes-8-1853-2023 (cit. on p. 27).

[30] T. Von Kármán and J.M. Burgers. *Aerodynamic Theory: General aerodynamic theory : Perfect fluids / [By] Th. von Kármán ; J. M. Burgers*. v. 2. J. Springer, 1935. URL: https://books.google.it/books?id=RC0HaAEACAAJ (cit. on p. 27).

[31] E. Branlard, J. Jonkman, B. Lee, B. Jonkman, M. Singh, E. Mayda, and K. Dixon. «Improvements to the Blade Element Momentum Formulation of OpenFAST for Skewed Inflows». In: *Journal of Physics: Conference Series* 2767 (2024). DOI: 10.1088/1742-6596/2767/2/022003 (cit. on p. 34).

[32] M. F. Howland, C. M. González, J. J. Pena Martínez, J. Bas Quesada, F. P. Larrañaga, N. K. Yadav, J. S. Chawla, and J. O. Dabiri. «Influence of atmospheric conditions on the power production of utility-scale wind turbines in yaw misalignment». In: *Journal of Renewable and Sustainable Energy* 12 (Dec. 2020). DOI: 10.1063/5.0023746 (cit. on p. 34).

[33] M. Sirigu, E. Faraggiana, A. Ghigo, and G. Bracco. «Development of MOST, a fast simulation model for optimisation of floating offshore wind turbines in Simscape Multibody». In: *Journal of Physics: Conference Series* (2022). DOI: 10.1088/1742-6596/2257/1/012003. URL: https://iopscience.iop.org/article/10.1088/1742-6596/2257/1/012003 (cit. on pp. 37, 39).

[34] Howland Lab. *Reference implementation of the Unified Momentum Model for rotors*. URL: https://github.com/Howland-Lab/Unified-Momentum-Model (cit. on p. 37).

[35] MOREnergy Lab. *MOST User Guide*. Tech. rep. Politecnico di Torino, 2024. URL: https://github.com/MOREnergylab/MOST/blob/master/Docs/MOST_GUIDE.pdf (cit. on pp. 38, 40, 50).

[36] NREL. *OpenFAST*. URL: https://www.nrel.gov/wind/nwtc/openfast.html (cit. on p. 38).

[37] L. Cottura, R. Caradonna, A. Ghigo, R. Novo, G. Bracco, and G. Mattiazzo. «Dynamic Modeling of an Offshore Floating Wind Turbine for Application in the Mediterranean Sea». In: *Energies* (2021). DOI: 10.3390/en14010248. URL: https://www.mdpi.com/1996-1073/14/1/248 (cit. on pp. 39, 46).

[38] E. Faraggiana, M. Sirigu, A. Ghigo, G. Bracco, and G. Mattiazzo. «An efficient optimisation tool for floating offshore wind support structures». In: *Energy Reports* (2022). DOI: 10.1016/j.egyr.2022.07.036. URL: https://www.sciencedirect.com/science/article/pii/S2352484722013014 (cit. on p. 39).

[39] E. Petracca, E. Faraggiana, A. Ghigo, M. Sirigu, G. Bracco, and G. Mattiazzo. «Design and Techno-Economic Analysis of a Novel Hybrid Offshore Wind and Wave Energy System». In: *Energies* (2022). DOI: 10.3390/en15082739. URL: https://www.mdpi.com/1996-1073/15/8/2739 (cit. on pp. 39, 46).

[40] TEHA (The European House - Ambrosetti). *Floating Offshore Wind Community: Conceptual Map 2023*. URL: https://www.ambrosetti.eu/site/get-media/?type=doc&id=18618&doc_player=1 (cit. on p. 42).

[41] Aeolian (Atlante EOlico ItaliANo). *Italian wind map*. URL: https://atlanteeolico.rse-web.it/ (cit. on p. 42).

[42] Smart Islands. *Pantelleria*. URL: http://www.smartisland.eu/replicabilita/pantelleria.html (cit. on pp. 42, 43).

[43] Terna. *Pantelleria becomes "Smart Island": Renewables, energy efficiency and electric transport to protect the environment*. URL: https://www.terna.it/en/media/press-releases/detail/Pantelleria_becomes_Smart_Island_Renewables_energy_efficiency_and_electric_transport_to_protect_the_environment (cit. on p. 42).

[44] Wimby. *Pilot sites*. URL: https://wimby.eu/pilot-sites/ (cit. on p. 42).

[45] MOREnergy Lab. *Test Area in Pantelleria*. URL: https://morenergylab.polito.it/wind-offshore-technologies/ (cit. on p. 43).

[46] I. Kielichowska et al. «Study on the offshore grid potential in the Mediterranean region». In: *doi/10.2833/742284* (2020) (cit. on p. 43).

[47] *Global Wind Atlas*. URL: https://globalwindatlas.info/en (cit. on p. 44).

[48] EMODNet (European Marine Observation and Data Network). *EMODnet Bathymetry*. URL: https://www.emodnet.eu/bathymetry (cit. on p. 44).

[49] MarineTraffic. *Global Ship Tracking Intelligence*. URL: https://www.marinetraffic.com/en/ais/home/centerx:11.8/centery:36.9/zoom:11 (cit. on p. 45).

[50] J. Jonkman, S. Butterfield, W. Musial, and G. Scott. *Definition of a 5-MW Reference Wind Turbine for Offshore System Development*. Tech. rep. National Renewable Energy Laboratory (NREL), 2009 (cit. on pp. 45, 51).

[51] A. Ghigo, F. Niosi, B. Paduano, G. Bracco, and G. Mattiazzo. «Mooring System Design and Analysis for a Floating Offshore Wind Turbine in Pantelleria». In: Oct. 2022. DOI: 10.1115/GT2022-83219 (cit. on p. 46).

[52] ECMWF (European Centre for Medium-range Weather Forecasts). *Copernicus Climate Change Service, Climate Data Store, (2023): ERA5 hourly data on single levels from 1940 to present*. URL: https://cds.climate.copernicus.eu/datasets/reanalysis-era5-single-levels?tab=download (cit. on p. 46).

[53] B. J. Jonkman and M. L. Buhl. *TurbSim User's Guide*. Tech. rep. National Renewable Energy Laboratory (NREL), 2006. DOI: 10.2172/891594 (cit. on p. 50).

[54] W. H. Munk. In: *Coastal Engineering Proceedings* 1.1 (Jan. 1950), p. 1. DOI: 10.9753/icce.v1.1. URL: https://icce-ojs-tamu.tdl.org/icce/article/view/904 (cit. on pp. 61, 62).

[55] A. Subbulakshmi, Mohit Verma, M. Keerthana, Saptarshi Sasmal, P. Harikrishna, and Santosh Kapuria. «Recent advances in experimental and numerical methods for dynamic analysis of floating offshore wind turbines — An integrated review». In: *Renewable and Sustainable Energy Reviews* 164 (2022), p. 112525. ISSN: 1364-0321. DOI: https://doi.org/10.1016/j.rser.2022.112525. URL: https://www.sciencedirect.com/science/article/pii/S1364032122004269 (cit. on p. 63).

[56] World Meteorological Organization. *Guide to Wave Analysis and Forecasting.* Guide to Wave Analysis and Forecasting. Secretariat of the World Meteorological Organization, 1988. ISBN: 9789263107022. URL: https://books.google.it/books?id=fN4aAQAAIAAJ (cit. on p. 62).

[57] M. S. Longuet-Higgins. *On the Statistical Distribution of the Heights of Sea Waves.* Journal of Marine Research, 1952 (cit. on p. 64).

[58] R. Picard. «Fourier Analysis». In: *International Encyclopedia of the Social Behavioral Sciences*. Ed. by Neil J. Smelser and Paul B. Baltes. Oxford: Pergamon, 2001, pp. 5754–5760. ISBN: 978-0-08-043076-8. DOI: https://doi.org/10.1016/B0-08-043076-7/00603-3. URL: https://www.sciencedirect.com/science/article/pii/B0080430767006033 (cit. on p. 65).

[59] C. L. Bretschneider. «Wave variability and wave spectra for wind generated gravity waves». In: 1959. URL: https://api.semanticscholar.org/CorpusID:119913545 (cit. on p. 65).

[60] W.J. Pierson and L. Moskowitz. «A proposed spectral form for fully developed wind seas based on the similarity theory of S.A. Kitaigorodskii». In: *Journal of Geophysical Research* (1963). DOI: https://doi.org/10.1029/JZ069i024p05181 (cit. on p. 65).

[61] K. Hasselmann et al. «Measurements of wind-wave growth and swell decay during the Joint North Sea Wave Project (JONSWAP)». In: *Deut. Hydrogr. Z.* 8 (Jan. 1973), pp. 1–95 (cit. on p. 65).